Mon. Not. R. Astron. Soc. **000**, 000–000 (0000) Printed 8 October 2006 (MN LATEX style file v1.4)

The first generation of stars in the ΛCDM cosmology

L. Gao[1,2⋆], T. Abel[3], C. S. Frenk[1], A. Jenkins[1], V. Springel[2], N. Yoshida[4]

[1] *Institute for Computational Cosmology, Department of Physics, University of Durham, South Road, Durham, DH1 3LE*
[2] *Max–Planck–Institut für Astrophysik, D-85748, Garching, Germany*
[3] *Kavli Institue for Particle Astrophysics and Cosmology, Standford University, 2575 Sand Hill Road, MS 29, Menlo Park, CA 94205, USA*
[4] *Department of Physics, Nagoya University, Furocho, Nagoya, Aichi 464-8602, Japan*

8 October 2006

ABSTRACT

We have performed a large set of high-resolution cosmological simulations using smoothed particle hydrodynamics (SPH) to study the formation of the first luminous objects in the ΛCDM cosmology. We follow the collapse of primordial gas clouds in eight early structures and document the scatter in the properties of the first star-forming clouds. Our first objects span formation redshifts from $z \sim 10$ to $z \sim 50$ and cover an order of magnitude in halo mass. We find that the physical properties of the central star-forming clouds are very similar in all of the simulated objects despite significant differences in formation redshift and environment. This suggests that the formation path of the first stars is largely independent of the collapse redshift; the physical properties of the clouds have little correlation with spin, mass, or assembly history of the host halo. The collapse of proto-stellar objects at higher redshifts progresses much more rapidly due to the higher densities, which accelerates the formation of molecular hydrogen, enhances initial cooling and shortens the dynamical timescales. The mass of the star-forming clouds cover a broad range, from a few hundred to a few thousand solar masses, and exhibit various morphologies: some have disk-like structures which are nearly rotational supported; others form flattened spheroids; still others form bars. All of them develop a single protostellar 'seed' which does not fragment into multiple objects up to the moment that the central gas becomes optically thick to H_2 cooling lines. At this time, the instantaneous mass accretion rate onto the centre varies significantly from object to object, with disk-like structures having the smallest mass accretion rates. The formation epoch and properties of the star-forming clouds are sensitive to the values of cosmological parameters.

Key words: methods: cosmology: theory – early universe – galaxies: formation – hydrodynamics – molecule processes – stars: formation

1 INTRODUCTION

The first generation stars, often referred to as "Population-III" stars, are thought to be the first sources of light in our Universe and the origin of the heavy elements required for the subsequent formation of ordinary stellar populations. Their remnant black holes may be the seeds from which supermassive black holes grow, including those that power quasars at redshift ~ 6 (e.g. Fan et al. 2003), when the Universe was just ~ 800 million years old. In the standard ΛCDM cosmology with a high amplitude of initial density perturbations, $\sigma_8 = 0.9$, the first stars are predicted to form at redshifts of about 20 and higher, based on the argument that gas in 3σ-halos at such redshifts should be able to cool and condense by molecular hydrogen cooling. Recent determinations of the cosmological parameters, obtained by combining the 2dFGRS galaxy power spectrum with the first and/or third year WMAP data (Sanchez et al 2005, Spergel et al. 2006), give a lower value of $\sigma_8 \sim 0.75$, implying that the formation epoch of the first stars could be as late as $z \sim 10$, opening the possibility that these stars may be detected directly by the next generation of space-borne and ground-based telescopes.

From a theoretical point of view, the formation of the first stars is a well-defined problem. Quantum fluctuations imprinted during the inflationary epoch provide the initial seeds for the formation and growth of the dark matter halos that host the first stars. In the absence of heavy elements, the only efficient coolant that can promote the formation of primordial star-forming gas clouds is molecular hydrogen (Peebles & Dicke 1968; Matsuda, Sato, Takeda 1969). Thus once the cosmological parameters and the fluctuation spec-

⋆ Email: liang.gao@durham.ac.uk

© 0000 RAS

trum are specified, the formation of the first luminous objects in the universe becomes, in principle, a straightforward physics problem.

Over the past decades, much progress has been achieved in following this program. Early studies used semi-analytical methods (e.g. Doroshkevich, Zel'Dovich & Novikov 1967; Peebles & Dicke 1968; Couchman & Rees 1986; Tegmark et al. 1997), while others utilised direct numerical simulations, either in one dimension (Haiman & Thoul & Loeb 1996; Omukai & Nishi 1998; Nakamura & Umemura 2001) or in three dimensions (Abel, Bryan & Norman 2000, 2002, hereafter ABN02; Bromm et al. 1999, 2002; Fuller & Couchman 2000; Yoshida et al. 2003, 2006; O'Shea & Norman 2006a,b). While the semi-analytical calculations have been instrumental in sketching out the relevant physics, the numerical simulations have been able to deliver detailed predictions for the outcome of the coupling between the chemo-thermal evolution and gravitational collapse. Comprehensive reviews of recent progress on the formation of the first luminous objects and associated radiative feedback processes may be found in Barkana & Loeb (2001), Bromm & Larson (2004), Glover (2005) and Ciardi & Ferrara (2005), and Ripamonti & Abel (2005).

Pioneering three-dimensional simulations of the formation of the first objects including non-equilibrium chemistry suggested that the first stars could be more massive than $100\,\mathrm{M}_\odot$ (Abel, Bran & Norman 1997; 2000; 2001; Bromm et al. 1999, 2002;). ABN02 employed cosmological initial conditions and adaptive mesh refinement (AMR) techniques to follow a star-forming gas cloud until it reached a central hydrogen number density, $n_\mathrm{H} \sim 10^{10}\mathrm{cm}^{-3}$, the point at which the assumption that the gas is everywhere optically thin breaks down and a radiative transfer calculation is required. Recently, Yoshida et al. (2006) included the effect of molecular line opacities and followed the further collapse of the central core to $\mathrm{n_H} \sim 10^{16}\mathrm{cm}^{-3}$. Bromm et al. (2002) (hereafter BCL02) and Bromm & Loeb (2005) used constrained initial conditions and smooth particle hydrodynamics (SPH) to study the same problem. Their simulations agree with those of ABN02 on many of the properties of the resulting star-forming cloud, but they also differ in a number of details.

A major disagreement is that ABN02 proposed that only one star forms per halo, whilst BCL02 argued that multiple stellar systems can form if the gas has sufficient initial rotation. In the latter case, the gas first collapses into a disk-like structure which fragments into several clumps very quickly. These clumps will then make their own stars if they can survive negative feedback effects from more advanced neighbouring clumps. Since ABN02 only simulated one particular object and the initial set-up of BCL was not realistic, there is hope that progress can be made by carrying out a number of simulations with realistic initial conditions in order to establish the typical properties of star-forming clouds and their variation.

One important caveat for simulations of the first stars has been noted by White & Springel (2000) and Gao et al. (2005) (hereafter G05). They argue that the first halos of any given mass do not form in 'typical' regions, but rather in 'protocluster' regions corresponding to peaks of the large-scale density field in the early universe. Since a significant contribution to the local overdensity at the sites of first star formation comes from megaparsec and larger wavelength fluctuations, some conclusions about the first objects reached from simulations of small volumes (which represent 'typical' regions) may be misleading. In particular, the formation redshift of the first halos of any given mass or temperature will be systematically underestimated.

G05 carried out a sequence of N-body re-simulations to follow the growth of one of the most massive progenitors of a supercluster region, from redshift $z \sim 80$, when its mass was just $10\,\mathrm{M}_\odot$, to the present epoch. They found that the mass of the first object reaches $10^5\mathrm{M}_\odot$ already at $z \sim 50$. A follow-up study of Reed et al. (2005) grafted a semi-analytical model developed by Yoshida et al. (2003) onto the dark matter merger trees of the G05 simulations and concluded that the first halo in this sequence of simulations would make one or more stars already at $z \sim 47$. Very rare objects like the one simulated by G05 are different from those formed in typical regions. These rare objects reside in extremely dense environments and experience particularly rapid growth. Their higher collapse redshift results in a higher initial density than in a typical region and this could result in significantly different evolution later on because the dynamical time, the cooling time, and the reaction rates for the formation of molecular hydrogen all depend on gas density. It is therefore an interesting question whether the formation paths and properties of star-forming clouds in these very rare objects are at all similar to those forming later on in more typical environments.

In this paper, we address this issue by asking two important questions: (1) *Is there a significant scatter in the properties of primordial star-forming clouds?* (2) *Do the properties of star-forming clouds depend on formation redshift?* We perform simulations of a sample of 8 first objects. By following evolution from different sets of initial conditions we can simulate a variety of formation redshifts and investigate the redshift dependence of the formation process.

This paper is structured as follows. In Section 2, we briefly introduce the chemical processes that are important for primordial gas. In Section 3, we describe our simulations. In Section 4, we take three of them as examples to sketch a general picture for the formation path of the first stars and then focus on one of them in greater detail. In Section 5, we study whether the properties of the star-forming clouds depend on collapse redshift and, in Section 6, we investigate how the baryon fraction influences the formation of the first stars. In Section 7, we discuss the abundance of star-forming halos. Finally, we give a summary of our results and set out our conclusions in Section 8.

2 PRISTINE GAS CHEMISTRY

In this section, we briefly summarize the basic gas processes that are important for primordial gas unpolluted by metals. Full details are given by Abel et al. (1997), Galli & Palla (1998) and Yoshida et al. (2006). For simulations that start at very high z, we now also include photo-reactions with cosmic microwave background (CMB) photons. At high redshift, in the absence of metals and when the temperature of gas in halos is lower than 10^4 K (above which atomic hydrogen line cooling is dominant), the principal coolant that can enable gas to condense into stars is the H_2 molecule.

The formation of molecular hydrogen has 3 main channels. At high redshifts, $z > 200$, the H_2^+ channel given by

$$H^+ + H \rightarrow H_2^+ + \gamma$$
$$H_2^+ + H \rightarrow H_2 + H^+$$

is dominant (but see Hirata & Padmanabhan (2006) for a different viewpoint). At these early times, there are sufficient numbers of energetic CMB photons to destroy H^- ions rapidly, so that a second possible channel,

$$H + e^- \rightarrow H^- + \gamma$$
$$H^- + H \rightarrow H_2 + e^-$$

is initially strongly suppressed. However, as the Universe expands and the CMB photons become less energetic, the H_2^- channel eventually becomes the main mechanism for creating molecular hydrogen. In this process, the residual electrons left unattached after recombination act as a catalyst.

When the density of gas exceeds $n_{\rm H} \sim 10^8 {\rm cm}^{-3}$, a third channel becomes important, through the three-body reaction:

$$H + H + H \rightarrow H_2 + H,$$
$$H + H + H_2 \rightarrow H_2 + H_2.$$

At sufficiently high densities, this reaction can, in fact, convert almost all atomic hydrogen into molecular form in a very short time. Our simulation code follows reactions for 9 species (e^-, H, H^+, He, He^+, He^{++}, H_2, H_2^+, H^-), including these H2 formation processes.

The cooling function for molecular hydrogen can be expressed as

$$\Lambda({\rm n_H, T}) = \frac{\Lambda_{\rm LTE}({\rm T})}{1 + \frac{\Lambda_{\rm LTE}({\rm T})}{{\rm n_H}\Lambda_{{\rm n_H}\rightarrow 0}({\rm T})}}, \quad (1)$$

where $\Lambda_{\rm LTE}$ and $\Lambda_{{\rm n_H}\rightarrow 0}$ are the cooling functions for high and low density limits. We adopt the high density limit given by Hollenbach & McKee (1979), assuming local thermal equilibrium (LTE), and the low density limit of Galli & Palla (1998). The transition between these two regimes occurs approximately at a gas density of $n_{\rm H} \sim 10^4 {\rm cm}^{-3}$. Above this value, the cooling rate per hydrogen molecule is independent of density, while below it, it is proportional to density.

3 SIMULATIONS

We have carried out a suite of simulations designed to study the formation of the first stars. For the first series, a standard ΛCDM cosmology, with matter, baryon and dark energy density parameters, $\Omega_m = 0.3$, $\Omega_b = 0.04$, $\Omega_\Lambda = 0.7$ respectively, and a Hubble constant $h_{100} = 0.7$, was adopted. The initial power spectrum was generated with CMBFAST and normalised to give an *rms* linear fluctuation amplitude of $\sigma_8 = 0.9$ in $8\,h^{-1}$Mpc tophat spheres at $z = 0$. The initial ionisation fraction was computed using RECFAST (Seager, Sasselov & Scott 2000).

One of the simulations used in this study has been previously analysed extensively by G05 and Reed et al. (2005). This simulation was constructed through a sequence of resimulations of the most massive progenitors of a supercluster region. Here we briefly describe the multi-grid procedure devised by G05:

(1) Identify a rich cluster size halo at $z = 0$ in a cosmological simulation of a very large volume ($\sim 1{\rm Gpc}^3$).
(2) Resimulate the evolution of this rich cluster and its environment with higher mass resolution.
(3) Determine the most massive object in the high resolution region of the re-simulation as a function of redshift, and identify the time when it first contains more than 10000 particles inside the viral radius.
(4) Resimulate the evolution of this progenitor object and its immediate surroundings with a further improvement in mass and force resolution.
(5) Iterate steps 3 and 4 until the desired redshift and progenitor mass are reached.

Following this procedure through 5 levels of resimulation, G05 were able to resolve a massive progenitor of the supercluster region capable of efficient H_2-molecular cooling at redshift $z \sim 50$. Their final, highest-resolution simulation had a particle mass of $1.08{\rm M}_\odot$ and is labelled "R5." Here we have re-ran "R5," this time including radiative cooling by molecular hydrogen and non-equilibrium chemistry. This is one of the main simulations analysed in this paper.

We carried out two additional simulations drawn from a periodic box of $300\,h^{-1}$kpc on a side. As noted by G05, the use of periodic boundary conditions suppresses fluctuations with wavelength longer than the side of the computational box. Therefore, if the box size is small, the appearance of a halo that could host first stars will be significantly delayed compared to a simulation of a larger volume. Our main motivation for simulating these two small periodic boxes is to enable us to compare our results to earlier studies carried out in this way (e.g. ABN02). In addition, however, since the formation of the first stars could plausibly span a wide range in redshift, our two small periodic box simulations are still interesting for studying first star formation at comparatively low redshifts.

In order to achieve sufficient resolution, we again utilised a resimulation technique similar to that of G05. First, we performed a simulation of a $300\,h^{-1}$kpc cubic region using 256^3 particles. We then identified the most massive objects at redshift $z \sim 15$ which typically have mass of $\sim 10^6 {\rm M}_\odot$ and resimulated them with a resolution comparable to the R5 simulation. Note that since the dynamic range of this simulation is much smaller than that of R5 (the initial volume is a factor 4×10^9 smaller), only one level of refinement, rather than five, is required to create the initial conditions of the final target simulation. Table 1 summarizes the principal numerical parameters of these simulations.

Since uncertaintes remain on the values of the cosmological parameters which describe our Universe, we have also rerun all the simulations listed in Table 1 adopting the parameters given in Table 5 of Spergel et al. (2006), derived from the combination of 3 years WMAP microwave data with the 2dFGRS galaxy power spectrum (Cole et al. 2005). We retain the same phases in the initial conditions but adjust the amplitudes of the modes according to the new power spectrum shape and normalisation. These cosmological parameters are significantly different from the values adopted in our other simulations: $\Omega_m = 0.236$, $\Omega_\Lambda = 0.764$, $\Omega_b = 0.042$

	R5	Z1	Z2
$m_{\rm dm}[{\rm M}_\odot]$	1.08	3.1	2.12
$m_{\rm gas}[{\rm M}_\odot]$	0.166	0.48	0.326
$M_{200}[{\rm M}_\odot]$	2.21×10^5	3.75×10^5	6.18×10^5
$z_{\rm end}$	47.91	25.9	21.0

Table 1. Numerical parameters of our first set of simulations. Here $m_{\rm dm}$ is the mass of each dark matter particle, while $m_{\rm gas}$ is the mass of each gas particle; $z_{\rm end}$ is the time when the central density of the gas cloud reaches $\sim 10^{10}$ when the optically thin assumption breaks down; M_{200} is the halo mass defined as the enclosed mass in a sphere of mean interior overdensity 200 times the cosmic mean density at the final time. This simulation series was performed using the standard cosmological parameters, $\Omega_m = 0.3$, $\Omega_\Lambda = 0.7$, $\Omega_b = 0.04$, $h_{100} = 0.7$, $\sigma_8 = 0.9$, with a primordial power spectrum index of $n_s = 1$.

	R5wt	Z1wt	Z2wt
$m_{\rm dm}[{\rm M}_\odot]$	0.77	2.22	1.52
$m_{\rm gas}[{\rm M}_\odot]$	0.167	0.48	0.328
$M_{200}[{\rm M}_\odot]$	4.42×10^5	1.16×10^6	2.55×10^6
$z_{\rm end}$	30.04	13.43	10.33

Table 2. Numerical parameters of our second set of simulations. The values of the cosmological parameters were taken from Table 5 of Spergel et al. (2006): $\Omega_m = 0.234$, $\Omega_\Lambda = 0.764$, $\Omega_b = 0.042$, $h_{100} = 0.73$, $\sigma_8 = 0.74$, and $n_s = 0.95$. The meaning of the tabulated quantities is the same as in Table 1.

and $h_{100} = 0.73$. The primordial power spectrum slope index is $n_s = 0.95$, and the normalisation is $\sigma_8 = 0.74$. Further details of this set of simulations are given in Table 2.

We performed a third set of controlled simulations to complement the other two. By design, these simulations form stars at redshifts intermediate between those of the first and the second sets. To achieve this, we ran additional versions of Z1 and Z2, with a lower value of $\sigma_8 = 0.74$, but employing the standard power spectrum, in order to increase the power on small scales, whilst the other cosmological parameters were set according to the 3rd year WMAP results. These simulations are detailed in Table 3.

Finally, we carried out simulations with both a higher and a lower baryon fraction than in the Z1 simulation in order to investigate how this parameter influences the formation of the first stars. For the higher baryon fraction case, we chose $f_b = \Omega_b/\Omega_m = 0.178$ which is consistent with the

	Z1w	Z2w
$m_{\rm dm}[{\rm M}_\odot]$	2.22	1.52
$m_{\rm gas}[{\rm M}_\odot]$	0.48	0.328
$M_{200}[{\rm M}_\odot]$	4.94×10^5	6.9×10^5
$z_{\rm end}$	20.65	16.75

Table 3. Parameters of simulations where the three-year WMAP cosmological parameters are adopted, but the shape of a standard cosmology power spectrum is retained.

	Z1hb	Z1lb
$m_{\rm dm}[{\rm M}_\odot]$	2.94	3.36
$m_{\rm gas}[{\rm M}_\odot]$	0.63	0.21
$M_{200}[{\rm M}_\odot]$	3.25×10^5	6.9×10^5
f_b	0.178	0.06
$z_{\rm end}$	26.26	24.26

Table 4. Numerical parameters of our simulations where we explored a higher and lower baryon fraction version than used in our default simulation of the Z1 object. The standard cosmology is assumed.

3-year WMAP cosmology while, for the lower baryon fraction case, we adopted $f_b = 0.06$ which matches the value used by ABN02 (for their assumed standard $\Omega_m = 1$ CDM cosmology). This allows a more direct comparison of their results with ours. See Table 4 for more information about these two simulations.

For all our simulations we used a fixed comoving gravitational softening length for dark matter particles equal to 1/30 of the mean interparticle separation, while for gas particles the gravitational softening was set equal to the SPH smoothing length. We experimented with a fixed gravitational softening length for gas particles, but this caused serious numerical problems for collapse simulations such as those presented in this paper (Bate & Burkert 1997; Abel et al., in preparation). Our simulations were performed with the widely used cosmological TreeSPH-code GADGET2 (Springel 2005).

4 FORMATION PATH OF THE FIRST STARS

After recombination, the temperature of the cosmic gas remains initially coupled to that of the radiation due to the presence of a small residual fraction of free electrons. After $z \sim 120$, this coupling becomes weak and the intergalactic medium (IGM) temperature starts to fall adiabatically as $T \propto (1+z)^2$ (e.g. Peebles 1993). While the assembly of cold dark matter into halos proceeds hierarchically starting at tiny mass scales, the accretion of gas into halos is affected by thermal pressure (e.g. Yoshida, Sugiyama, & Hernquist 2003). The density of gas only rises significantly above the mean cosmic gas density within halos that have a mass comparable or greater than the Jeans' mass $M_{\rm J} = 4/3\pi^{5/2} c_s^3 (G\rho)^{-3/2}$, where c_s is the sound speed of the gas, and ρ is the density.

Once a dark matter halo becomes massive enough for its baryon content to overcome the thermal gas pressure, it can accrete enough material to reach a baryon fraction close to the universal value. When the temperature is high enough (~ 1000K), the processes described in Section 2 can promote the formation of molecular hydrogen which then acts as a coolant. A runaway cooling and compression process begins at the halo centre, the details of which are the main topic of this and the next section. When the central density of hydrogen reaches values of around $n_{\rm H} \sim 10^{10}{\rm cm}^{-3}$, the gas ceases to be optically thin to the molecular hydrogen lines. At this point, our simulations are no longer able to follow the collapse process any further in a physically meaningful

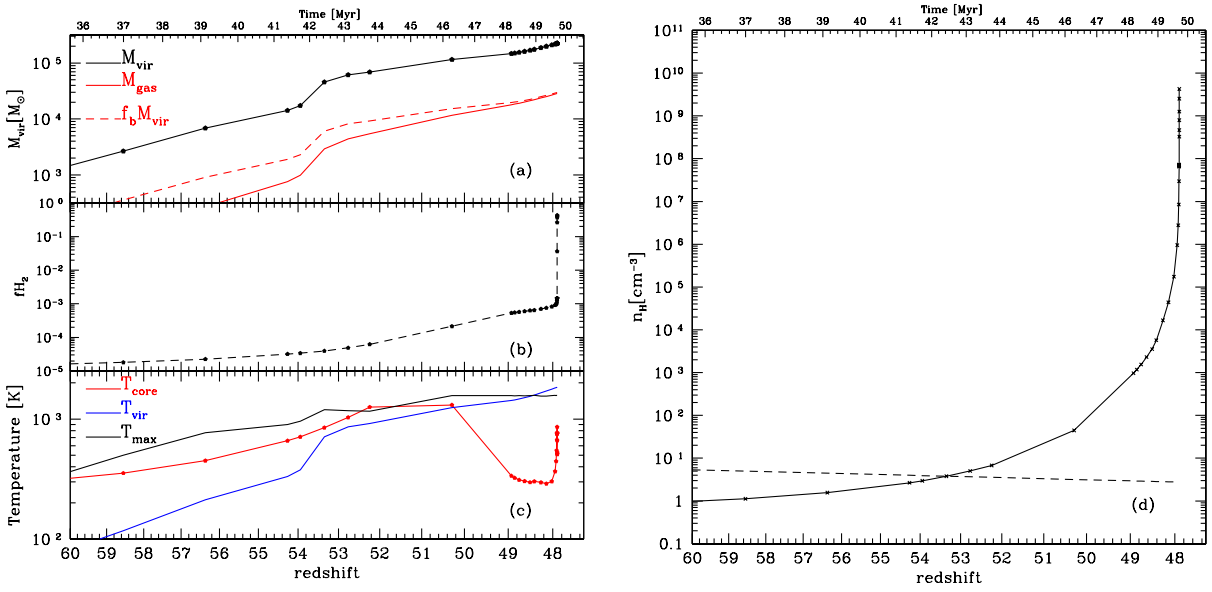

Figure 1. Evolution of different physical properties of the 100 SPH particles ($\sim 20\,\mathrm{M}_\odot$) which end up closest to the centre of the halo at the final output time. Panel (a): the black solid lines with symbols show the virial mass of the main halo progenitor; the lower (red) solid lines show the mass of the gas component within the virial radius of the halo; the (red) dashed lines are the fiducial gas mass that the halo would contain at the universal baryon fraction, $f_b = \Omega_b/\Omega_m$. Panel (b): the evolution of the H_2-fraction for the 100 selected gas particles. Panel (c): the gas temperature evolution. The lower (blue) solid line is an estimate of the virial temperature of the main halo, as described in the text; the black solid lines are the maximum temperature defined as the maximum of the spherically mass-averaged temperature profile of the the gas in the main halo. The (red) solid lines with symbols show the evolution of the median value of the temperature for the 100 selected particles. Panel (d): the solid lines with symbols are the median values of the number density of hydrogen nuclei in the 100 selected particles. The dashed lines indicate 200 times the cosmological mean number density.

way because the appropriate radiative transfer processes are not modelled. For the purposes of our analysis we therefore define the final time of our simulations to be the point where the central density reaches a value of $n_{\rm H} \sim 10^{10}{\rm cm}^{-3}$.

In the following subsections, we illustrate the path leading to the first stars by discussing three of our simulations, R5, Z1, and Z2wt, in detail. These form a comprehensive set in terms of the formation redshift of their first star: R5 is the first to produce a star-forming object, at a redshift of $z \sim 50$; in Z1 the halo collapses at an intermediate redshift of $z \sim 26$, close to what is often assumed in the literature to be the typical formation epoch of the first stars; Z2wt forms its first star as late as $z \sim 10$.

4.1 Overview of the formation of the first stars at the highest redshifts

A useful way to describe the formation path of the first stars is to track the evolution of the properties of gas particles that end up in the central region at the final time. To this end, we select the 100 innermost SPH particles which lie closest to the centre of the R5 halo at the end of the simulation. We take the centre of a halo to be the position of the minimum of the gravitational potential. Our results are quite similar when we consider the innermost 1000 particles instead.

The median values of various physical properties of the innermost 100 particles as a function of time are shown in Figure 1. Panel (a) shows the mass accretion history of the gas and dark matter components of the object in R5. The solid black line shows the evolution of the virial mass of the dominant halo. The virial mass is defined as the total mass within the spherical region around the centre that encloses a density of 200 times the mean cosmic value. The red dashed line is a fiducial gas mass, given by the gas mass that the dark matter halo would contain if it had the universal baryon fraction, $f_b = \Omega_b/\Omega_m$. The solid red line shows the actual gas mass within the virial radius. It is not surprising that at $z > 55$ the baryon fraction of the halo is much lower than the cosmic mean, because the gas thermal pressure keeps the gas out of the halo. The baryon fraction is less than 10% of the fiducial value at redshift $z = 60$ when the halo has a mass of $1000\,\mathrm{M}_\odot$, but rises to 65% at redshift $z = 50$ by which time the mass of the halo has grown to $10000\,\mathrm{M}_\odot$. The universal baryon fraction is approximately reached when the halo has grown to a mass of $10^5\,\mathrm{M}_\odot$, at $z \sim 49$.

Panel (b) shows the evolution of the molecular hydrogen fraction, $f_{\rm H_2}$, of the 100 selected gas particles, while panel (c) shows their temperature. For comparison, the blue solid line shows the estimated virial temperature of the halo,

$$T = \mu m_p\, V_c^2/(2\,k_{\rm B}), \qquad (2)$$

where $\mu\, m_p$ is the mean molecular weight of the gas, V_c is the circular velocity of the halo and $k_{\rm B}$ is Boltzmann's constant. The black solid line refers to the maximum temperature of the main object, determined by first binning the gas particles within the halo into concentric logarithmically spaced

shells centred on the potential minimum, then computing the mass-weighted temperature of each bin, and finally taking the maximum value of all the bins. The location of the maximum temperature roughly indicates where the accretion shock occurs.

The evolution of the number density of hydrogen nuclei for the selected 100 particles is shown in panel (d) as a solid line with symbols. The dashed line corresponds to 200 times the cosmic mean number density. The crossing point of the two curves roughly marks the time when these 100 gas particles settle into the virialised halo.

Based on these plots, we can outline a simple picture of how the gas cloud condenses to the point of forming the first star in the R5 halo. Prior to redshift $z \sim 53$, when the mass of the dark halo is less than $2 \times 10^4\,\mathrm{M}_\odot$, the virial temperature of the halo is substantially lower than that of the ambient IGM gas. (Note that the mean temperature of the surrounding IGM is higher than the cosmic mean of $T \sim 60\,\mathrm{K}$ because the R5 object resides in a significantly overdense region; see G05). In this phase, the gas accretion onto the R5 halo is limited by gas pressure. At $z \sim 53$, a major merger takes place and the mass of the halo nearly doubles. This significant increase in mass deepens the gravitational potential well, allowing gravity to overwhelm the gas pressure, so that ambient gas starts to settle into the halo. This can be observed in panel (a) as a rapid increase in the baryon fraction at this redshift. The 100 selected gas particles settle into the halo as their density reaches the characteristic value of 200 times the cosmic mean required for virialization, as seen in panel (d).

The amount of molecular hydrogen increases by almost one order of magnitude from $z = 53$ to $z = 50$ due to the substantial increase in gas temperature as well as density. Further production of molecular hydrogen, however, is retarded by the depletion of electrons due to recombination, but the gas nevertheless continues to contract. Shortly before the gas density reaches $n_\mathrm{H} \sim 10^8\mathrm{cm}^{-3}$, three-body formation of molecular hydrogen becomes important and this results in very efficient cooling followed by runaway collapse. When the gas density reaches $\sim 10^{10}\mathrm{cm}^{-3}$, the gas becomes optically thick to H_2-cooling lines, and our simulation cannot proceed further in a physically meaningful way (see Yoshida et al. 2006 for a calculation of gas evolution beyond this point).

4.2 The formation of first stars at lower redshifts ($z = 25$ and $z = 10$)

The simulations labelled Z1 and Z2wt in Section 3 allow us to examine whether or not the formation paths of protostars at lower redshifts differ from those forming at high z. The first objects in these simulations form much later than in R5. In Z1 the first protostar forms at $z \sim 25$, which is often taken in the literature to be the typical formation redshift of primordial stars; in Z1wt the first protostar forms at $z \sim 10$, the lowest value in our sample.

We carry out a similar analysis for Z1 and Z2wt to that for the R5 object presented in Figure 1. We identify the innermost 100 SPH particles at the final simulation output and then trace these particles back to earlier times. The time evolution of the median values of various physical quantities in the Z1 and Z2wt simulations are shown in Figure 2.

On the whole, the formation paths of protostars in the Z1 and the Z2wt simulations are similar to those in R5. The baryon fraction in the halo is initially lower than the universal value but it then catches up, as in R5. However, the mass scale where this happens is smaller because the cosmological Jeans mass, $M_\mathrm{J}(z) \propto T^{3/2}\rho^{-1/2} \propto (1+z)^{3/2}$, is smaller at lower redshifts. After this stage, the gas is continuously compressed and its temperature raises, resulting in the rapid formation of H_2. When the gas temperature reaches $T \sim 1000\,\mathrm{K}$ and the H_2 fraction increases to a few times 10^{-4}, the gas begins to cool rapidly, just as in R5.

Despite the overall similarity of the formation paths of the first objects in Z1, Z2wt and R5, the timescale for collapse is very different. In R5 it takes only about 3 million years between the time when efficient cooling starts (signalled by the decline in temperature) to the time when the number density reaches $n_\mathrm{H} \sim 10^{10}\mathrm{cm}^{-3}$, but this phase takes 10 and 100 million years in Z1 and Z2wt respectively. The initial collapse of protostellar objects proceeds much more rapidly at very high redshift because of the higher density which accelerates the formation of molecular hydrogen, enhances initial cooling, and shortens the dynamical time.

These results suggest a relatively simple picture of the formation path of the first stars although the detailed evolution can be complicated and may differ from object to object depending on the particular infall pattern. As the halo virial temperature approaches a critical temperature, $T \sim 1000\,\mathrm{K}$, the rapid production of molecular hydrogen starts once the H_2 fraction reaches a critical value of a few times 10^{-4}, allowing the gas to cool efficiently. The timescale for the subsequent evolution to a protostar varies systematically depending on the redshift when the collpase is taking place, with halos at higher redshift collapsing faster. In our simulations the timescale varies by a factor as large as 20 between redshifts $z \sim 50$ and $z \sim 10$.

Panel (a) in Figures 1 and 2 also suggests that the virial temperature provides only a crude estimate of the gas temperature in the halos because the gas accretion process in the protostellar clouds is rather complicated. The maximum temperature, which marks the site of the accretion shock, can often differ significantly from the virial temperature. These two temperatures only roughly match at the time when the cosmic Jeans mass is reached, which is also the time when the baryon fraction in the halo becomes close to the universal value. After this, the maximum temperature is usually smaller than the estimated virial temperature by a factor as large as 50%.

Our results imply that a criterion for deciding whether or not a halo hosts a star-forming cloud based purely on the mass or virial temperature of the host halo, as used extensively in the literature, is unlikely to give the correct answer. While it is true that the gas starts to collapse and cool when the halo attains a virial temperature close to $\sim$ 1000 K, the processes eventually leading to the formation of a protostar can take a significant amount of time and this must be taken into account.

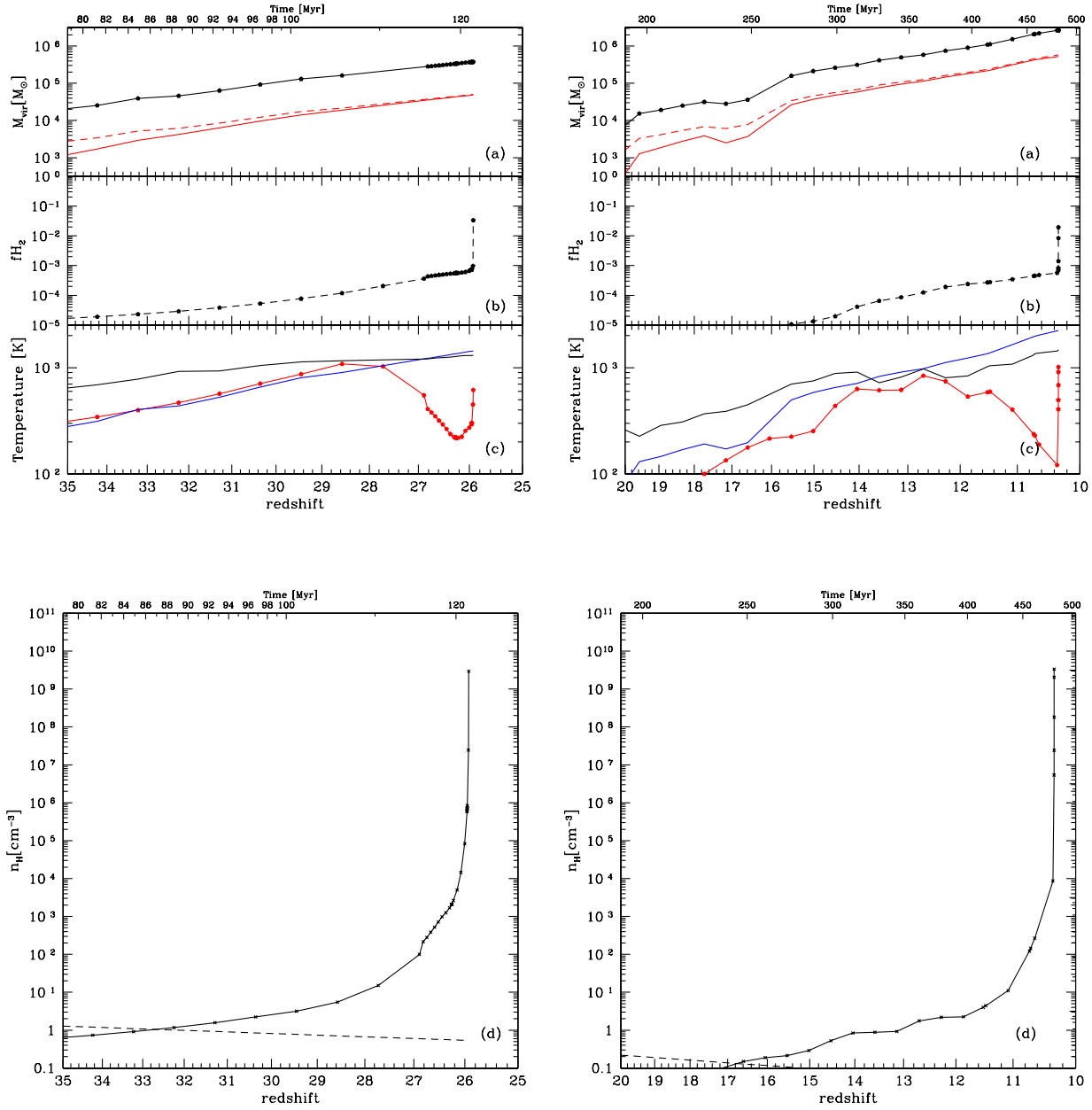

Figure 2. Evolution of various properties of the final innermost 100 SPH particles in the Z1 simulation (left panels) and the Z2wt simulation (right panels). Panel (a): the black solid lines with symbols show the virial mass of the main progenitor; the (red) solid lines show the mass of the gas component within the virial radius of the halo; the (red) the (red) dashed lines are the fiducial gas mass that the halo would contain at the universal baryon fraction, $f_b = \Omega_b/\Omega_m$. Panel (b): the evolution of the H_2 fraction of the final 100 innermost gas particles. Panel (c): the gas temperature evolution. The lower (blue) solid line is an estimate of the virial temperature of the main halo, as described in the text; the black solid lines are the maximum temperature defined as the maximum of the spherically mass-averaged temperature profile of the the gas in the main halo. The (red) solid lines with symbols show the evolution of the median value of the temperature for the 100 selected particles. Panel (d): the solid lines with symbols are the median values of the number density of hydrogen nuclei in the 100 selected particles. The dashed lines indicate 200 times the cosmological mean number density.

4.3 Star formation in the R5 simulation

4.3.1 The distributions of dark matter and gas

The distributions of dark matter density, gas density and mass-weighted temperature for the R5 object are shown, at three different epochs, in Figure 3. The images are of length $4\,r_{200}$ on a side and are projected over a depth of r_{200} centred on the potential minimum. Here r_{200} is defined as the virial radius of the dominant object at the final time. The scales on the axes give the length in physical units and

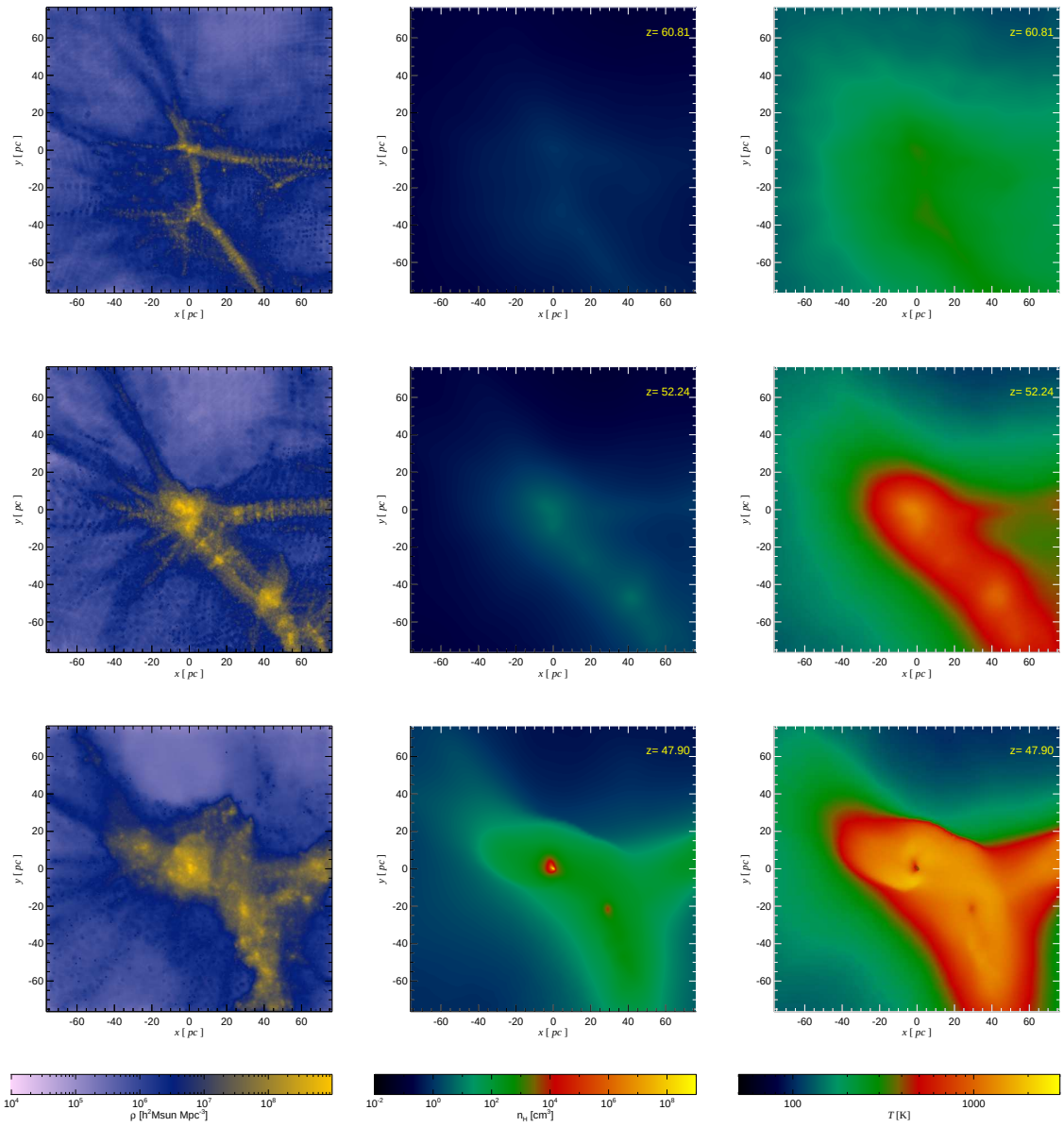

Figure 3. Projected dark matter density (left), gas density (middle) and gas temperature (right), weighted by mass at three redshifts in the R5 simulation. In all cases, the projected regions have dimensions of 4 times the virial radius of the R5 object in the plane of the plot and are projected over a depth of 1 virial radius at the final time.

a consistent colour table has been used within each column. The three epochs shown are representative of the system at the time when its mass is below the Jeans mass, close to the Jeans mass, and at the end, when runaway cooling is occurring at the centre. From left to right, the columns give the dark matter surface density in physical units, the gas density in physical units, and the mass-weighted gas temperature, respectively.

At redshift $z = 60$, the dark matter structure is very filamentary, as is typical in CDM models (e.g. Abel, Bryan & Norman 1998; Yoshida et al. 2003; G05). However, the gas is noticeably less clumpy than the dark matter. Nonetheless, the gas does get compressed due to the significant concentration of the dark matter. As a result, the entire region has a temperature of $\sim 300\,\mathrm{K}$, several times the temperature of $\sim 80\,\mathrm{K}$ expected for the cosmic mean density at that epoch.

At redshift $z = 52$, the dark matter structures are already much more pronounced than at $z = 60$. Following the rapid growth of the dark matter structures, the gas begins to settle into the dark matter halos; two dense gas clumps are clearly seen in the density map. The increase in gas density results in substantial heating of the gas due to compression. This can be seen in the large region around the filaments where the temperature is $\sim 600\,\mathrm{K}$. In the central region of the main dark matter halo, two small brighter regions are visible with temperature of $\sim 1000\,\mathrm{K}$.

The bottom panels show the system at the final time, when star formation is beginning in the innermost regions. Note that a second concentration is also evident at a distance

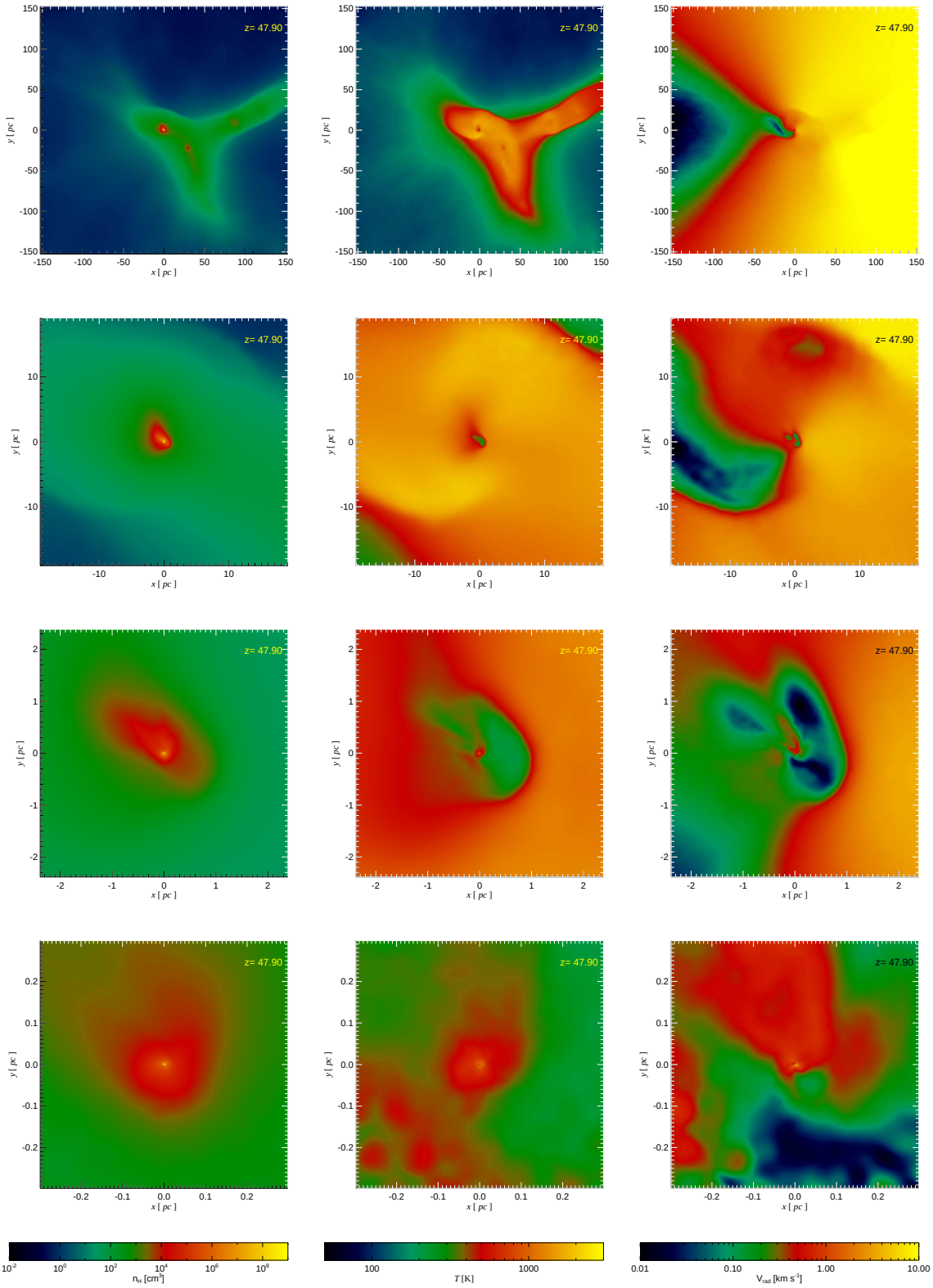

Figure 4. Projected gas density (left), mass-weighted temperarture (middle) and radial velocity with respect to the star-forming region, at the final time in the R5 simulation. The sequence of images in each column, from top to bottom, shows zooms by successive factors of 8 in linear scale onto the centre of the object.

of about 40 proper parsecs in projection. In the bottom-right panel, two shocks develop along the filaments. On a scale of $\sim 10\,\mathrm{pc}$, the shock around the dominant object is even more pronounced. Note that the shock occurs in the very inner regions rather than at the viral radius, $r_{\rm vir} = 35\,\mathrm{pc}$. Just inside the shock front, a molecular hyrdogen rich and rapidly cooling region is found.

A more detailed set of images of the R5 object at the final time is displayed in Figure 4. From left to right, the columns show surface density, mass-weighted temperature, and the radial velocity with respect to the star-forming core. From top to bottom, the images show successive zooms by factors of 8 in linear scale onto the centre of the gravitational potential at the final time. The radial velocity is defined as the velocity relative to the average velocity of the innermost 100 SPH particles. On small scales, the gas cloud reveals a complex structure, especially in the radial velocity map. The gas accretion is clearly asymmetrical. The infall velocity is much larger for the gas on the right hand side, where the secondary gas concentration is closing in towards the dominant object, accompanied by a one-sided accretion shock at a scale of $\sim 1\,\mathrm{pc}$. Clearly, describing these processes as spherically symmetric gas accretion is unrealistic.

4.3.2 Time evolution of radial profiles around the dominant object

The time evolution of the gas in the R5 object is described in Figure 5 which shows the mass-weighted radial profiles of various physical quantities of interest. We define the cooling timescale as $t_{\rm cool} = -\mathrm{d}t/\mathrm{d}\ln T$, where T is the gas temperature, and t is time. The free-fall time is defined as $t_{\rm ff} = 2\pi\sqrt{3/32G\rho}$, where ρ is the density. We show 6 epochs corresponding to $z = 52.24$, 50.29, 48.50, 48.02 and 47.91; the final epoch corresponds to $z = 47.90$.

We start 6.4 million years before the final time, at $z = 52.24$, when the R5 halo has only just reached the Jeans mass. Gravity is then strong enough to cause gas to settle into the potential well of the halo. By then, the central part of the gas distribution is heated to more than 1000 K. However, the cooling time is still much longer than the free-fall time because the gas density and molecular hydrogen fraction are still relatively low. At this stage, the gas contracts slowly. About 2.7 million years later, at $z = 50.29$, the central gas density has increased by a factor of 10, and the molecular fraction has also increased by a factor of 10. This results in a much shorter cooling time for the central $2000\,\mathrm{M}_\odot$ of gas, which is now comparable to the free-fall time. At this point, the gas cloud begins to collapse rapidly.

Another 2.7 million years later, at $z = 48.50$, the central $1000\,\mathrm{M}_\odot$ of gas approach the critical density, $n_{\rm H} \sim 10^4\mathrm{cm}^{-3}$, which marks the transition of H_2-cooling from NLTE rotational level populations to an LTE state. Above this density, the cooling rate per molecule of hydrogen becomes independent of density. The central gas temperature falls to close to 200 K, which is roughly the minimum temperature that can be reached by molecular hydrogen cooling. By now the production of molecular hydrogen has entered a regime where the abundance scales logarithmically with time due to the continuous depletion of electrons through recombination (Tegmark et al. 1997).

Finally, a further 1 million years later, at $z = 48.02$, the central gas density approaches the critical density required for three-body reactions, resulting in rapid H_2 formation and an increase of the gas temperature due to heating from both compression and the release of molecular binding energy. After 10^5 years, there is a substantial increase in the H_2 fraction in the central few hundred solar masses of gas with density exceeding $10^8\mathrm{cm}^{-3}$. As a consequence, the cooling time of the central $20\,\mathrm{M}_\odot$ of gas becomes shorter than the free-fall time, and the mass eventually exceeds the locally estimated Bonnor-Elbert mass (Elbert 1955; Bonnor 1956):

$$M_{\rm BE} \sim 20\mathrm{M}_\odot T^{3/2} n^{-1/2} \mu^{-2} \gamma^2. \quad (3)$$

Runaway collapse is triggered at this time. Here n is the number density of hydrogen nuclei, μ is the molecular weight and γ is the adiabatic index. Note that the Bonnor-Elbert mass is similar to the Jeans mass but it assumes an isothermal rather than an uniform gas distribution.

5 OBJECT-TO-OBJECT COMPARISONS: DIFFERENCENS AND SIMILARITIES

As we have seen in the previous section, the formation epoch of the first stars can span a broad redshift range, and there are systematic differences in the formation process of protostellar clouds that depend on redshift. An additional source of variation comes from the differences in the assembly histories of these objects at a given redshift (e.g. Lacey & Cole 1993). It is therefore important to analyse a number of realisations in order to assess the expected scatter in the properties of star-forming clouds. We now address this issue by jointly considering all of our simulations.

5.1 Radial profiles

Figure 6 shows the radial profiles of the density, enclosed gas mass, molecular hydrogen fraction and temperature in all our simulations. The comparison is made at the final time when the central gas has roughly reached the limiting density, $n_{\rm H} \sim 10^{10}\mathrm{cm}^{-3}$, in all the simulations. At this time, runaway collapse has set in and the minimum simulation timestep becomes extremely small. The top left panel shows the number density profile of hydrogen nuclei. Each object is represented by a different colour line as indicated in the top-left panel. A striking feature in this plot is that the gas density profiles of the objects in all our simulations coincide with one another on scales less than $\sim 10\,\mathrm{pc}$, in spite of their very different collapse redshifts and environments.

The scatter is remarkably small, only a factor of ~ 2 about the mean, which is smaller than in the simulations of O'Shea &Norman (2006b). For comparison, the red crosses and the blue dashed line show the fiducial density profiles of ABN02 and Yoshida et al. (2006), respectively. Our simulations agree well with ABN02 on scales smaller than 0.02 pc, but not very well at larger radii. As we will show in Section 6, the different baryon fractions assumed in the two studies largely account for this discrepancy. Yoshida et al. (2006), on the other hand, adopt the same cosmology as us. Our results agree well within 0.2 pc, but not as well on larger scales. This suggests that the actual variation in density profile from object to object may be bigger than indicated by the limited samples we have simulated here. The top right

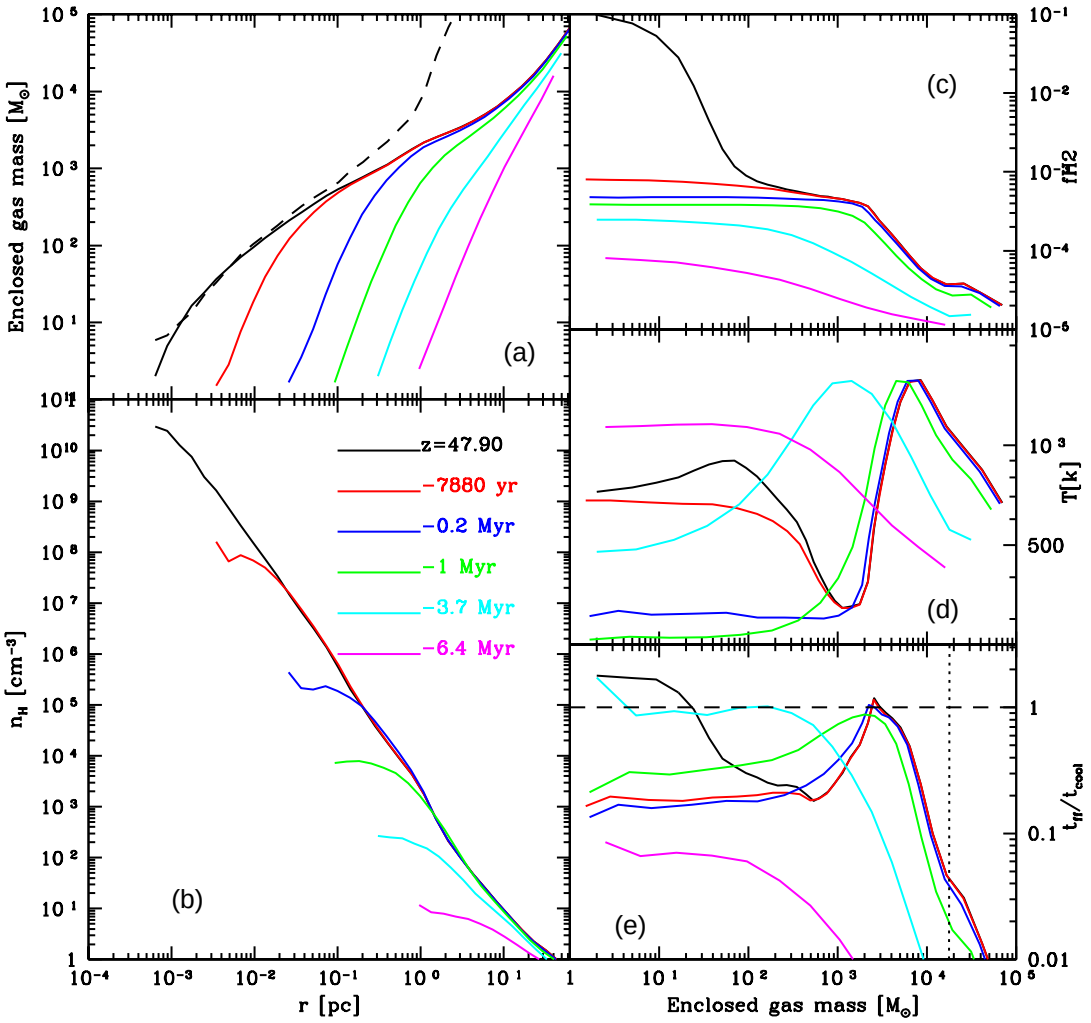

Figure 5. Radially averaged profiles of various physical quantities at different epochs in the R5 simulation. The colour lines refer to the epochs indicated in panel (b), where the time is expressed as the number of years before the final time, and the corresponding redshifts from top to bottom are: 47.90 (the final time), 47.91, $z = 48.02$, $z = 48.50$, $z = 50.29$, and $z = 52.24$. Panel (a): enclosed gas mass as a function of radius. Panel (b): number density profile of hydrogen nuclei. The dashed lines are the local Bonnor-Ebert mass, which is similar to the Jeans mass but assumes an isothermal rather than an adiabatic distribution for the gas. Panel (c): molecular hydrogen fraction as a function of the enclosed gas mass. Panel (d): gas temperature. Panel (e): the ratio of free-fall time to the cooling timescale. The vertical doted lines in all panels indicate the virial radius of the halo at the final time.

panel shows the enclosed gas mass as a function of radius, which also confirms the rather small variation in mass profile from object to object in our simulations.

The molecular hydrogen fractions in all our simulations also agree well with each other at radii less than 10 pc. The temperature structures are similar as well. The latter can be roughly divided into 4 physically distinct zones. Zone 1 is the outermost region and corresponds to cosmic infall, where the gas is continually heating up, culminating at the accretion shock front where the maximum temperature occurs. In the region immediately behind the shock front, which makes up zone 2, the gas temperature decreases inwards up to a radius, ~ 1 pc, where the temperature reaches a minimum of ~ 200 K, below which the molecular hydrogen cooling rate drops exponentially. Within this radius, in zone 3, there is a second infall region in which the temperature rises back up again and approaches 1000 K at a radius of ~ 0.01 pc. Here, the gas density reaches a value of $n_{\rm H} \sim 10^8 {\rm cm}^{-3}$. At this characteristic density, three-body reactions which rapidly form molecular hydrogen start to operate and the enhanced cooling associated with the rising molecular hydrogen fraction causes the temperature to decrease towards smaller radii temporarily. The temperature profiles are all qualitatively similar but they can be grouped into two classes: R5, R5wt, Z1w and Z2wt in one, and Z1, Z1wt, Z2, Z2w in the other. As we will see in the next sub-

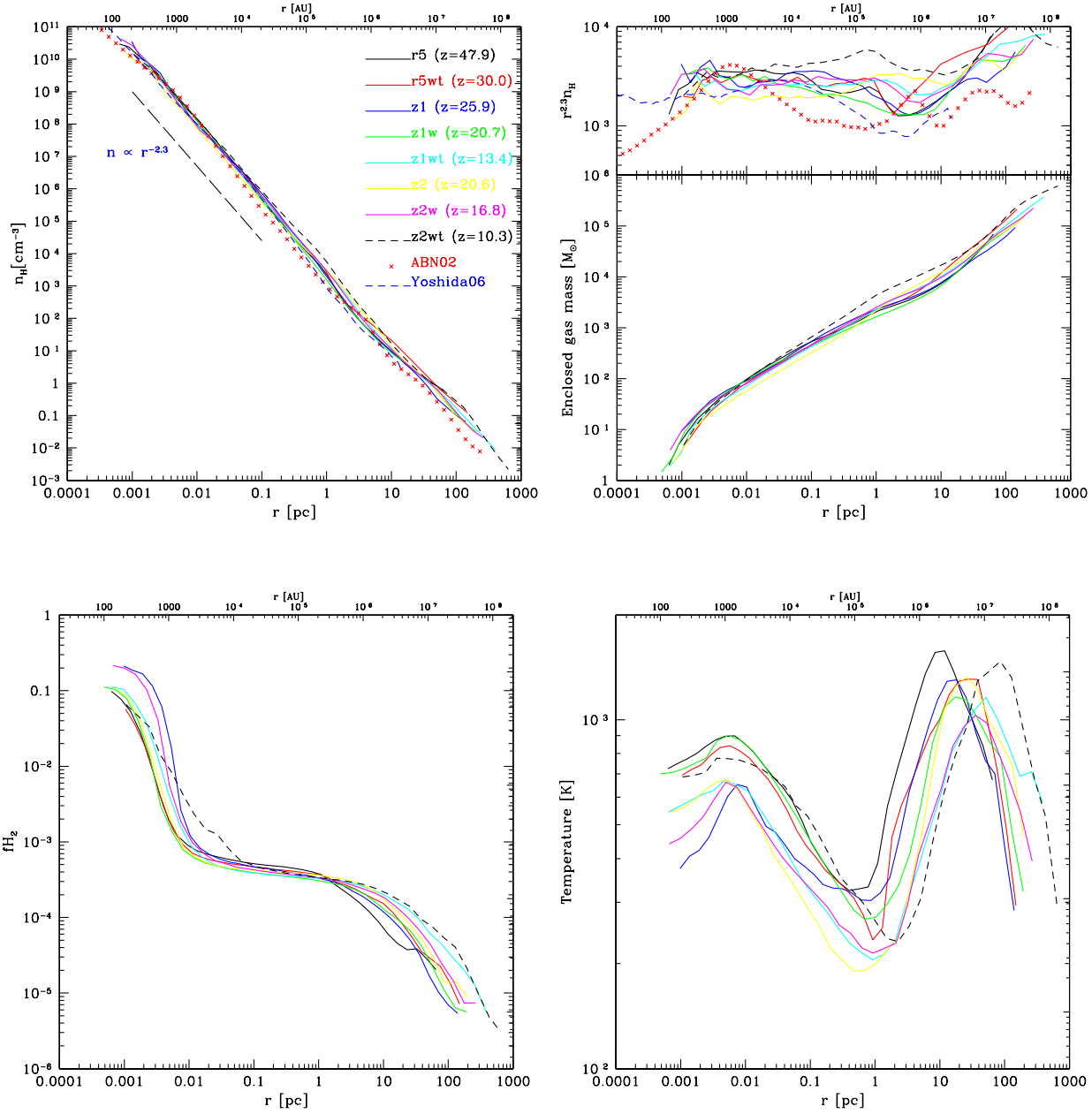

Figure 6. Radially averaged profiles of various physical quantities as a function of radius in the 8 simulations. The different lines refer to the different simulations as indicated by the labels in the top left-hand panel. Top left: number density of hydrogen nuclei. Top right: enclosed gas mass. Bottom left: molecular hydrogen fraction. Bottom right: gas temperature.

section, the star-forming clouds in the second group have a disklike structure. As a result, the collapse is slower and the competition between compressional heating and molecular hydrogen cooling results in a lower inner temperature.

Figure 7 compares the radial profiles of various dynamical quantities. Here, for clarity, we show results only for 3 typical simulations, R5, Z1 and Z2wt, which we analysed in Section 3. A complete version of the figure including all the other simulations may be found in the Appendix. Figure 7 reveals that despite the similarities in the gas properties seen in Figure 6, the internal gas motions differ dramatically from object to object. They are only similar in the cosmic infall region which terminates at the first accretion shock where the radial velocity (defined to be negative for infalling gas) reaches a local minimum and the temperature a local maximum. The mass inside this radius is about $10^4\,M_\odot$ for the R5 and Z1 objects, and $10^5\,M_\odot$ for the Z2wt object. For the R5 object, the gas infall velocity is relatively constant but declines rapidly at a radius corresponding to a mass scale of $10^3\,M_\odot$. Just inside this scale, the gas infall speeds up again. For the Z1 object, the infall speed increases just behind the accretion shock and reaches a local maximum at

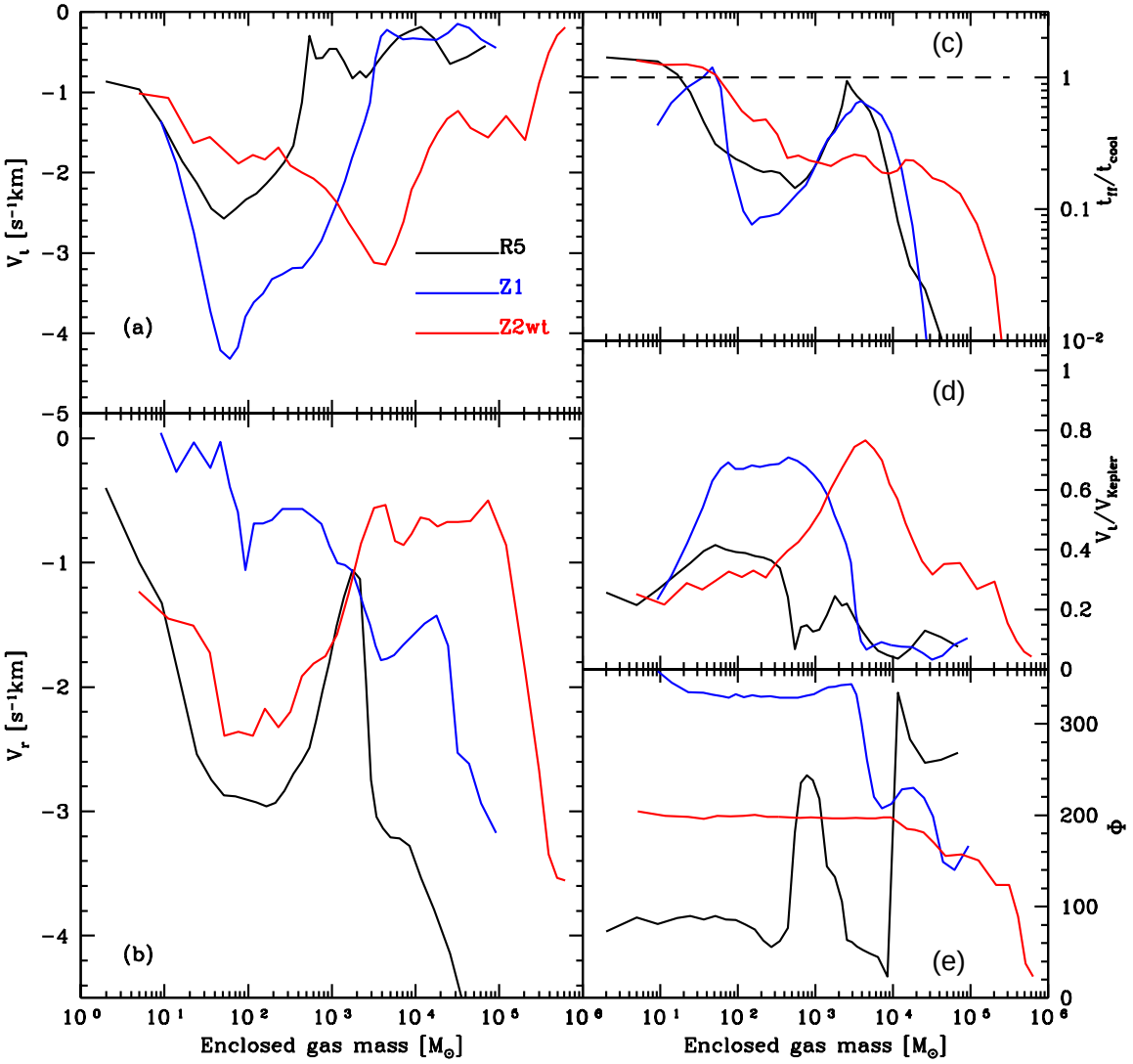

Figure 7. Radial profiles of various physical quantities as a function of the enclosed gas mass at the final time in 3 representative simulations: R5, Z1 and Z2wt. Panel (a): profiles of negative tangential velocity. Panel (b): radial velocity profiles. Panel (c): the ratio of the free-fall time to the cooling time. Panel (d): the ratio of the tangential velocity to the Keplerian velocity $v_{Kepler} = (GM/r)^{1/2}$. Panel (e): the orientation of the angular momentum. Note that only the angle ϕ is shown.

a mass scale of $3 \times 10^3\,\mathrm{M}_\odot$, where the ratio of the free-fall time to the cooling time is maximal (panel c). Exactly at the same scale, the tangential velocity starts to become larger than the infall velocity. For the Z2wt object, the radial velocity stays constant at large radii. At a mass scale of about $5 \times 10^3\,\mathrm{M}_\odot$, the radial infall velocity increases until a mass scale of a few tens of solar masses. Note that a jump in the ratio of the free-fall time to the cooling time often marks a transition in the velocity and orientation of the angular momentum.

Panel (d) gives the ratio of the actual tangential velocity of the gas to the velocity required for Keplerian motion, defined as $|\vec{V}_t|/V_{\mathrm{Keplerian}}$. The curves for the three simulations differ substantially, implying that the degree of rotational support is rather different. Finally, panel (e) shows the azimuthal angle between the z-axis in the simulation and the angular momentum vector of the gas interior to a given radius, or equivalently an enclosed mass. It is clear that the different parts of the halos often spin in different directions. For the R5 object, the gas only rotates in the same direction

inside an enclosed mass of $300\,M_\odot$, while the same is true for the Z1 and Z2wt halos inside $3000\,M_\odot$ and $10000\,M_\odot$, respectively. Comparing with the other panels in the Figure, we see that a jump in tangential velocity typically accompanies a jump in the orientation of the angular momentum.

5.2 Morphology of the star-forming clouds

In spite of the similarities in radial profiles seen in the previous subsection, the final star-forming clouds exhibit a variety of morphologies. We define the edge of the star-forming cloud as the largest radius inside which the orientation of the angular momentum of the enclosed material (determined by the azimuthal angle introduced in the previous subsection) does not change significantly. We then calculate the principal axratios, $q = b/a$ and $s = c/a$ (taking $a > b > c$), of the inertia tensor of all gas particles in the star-forming cloud. (These axial ratios may be viewed as the equivalent axial ratios of a homogeneous ellipsoidal distribution with the same inertia tensor as the gas distribution.) The axial ratios for all our simulated objects are given in Table 5. We also list here the ratio of the tangential velocity to the Keplerian velocity at the edge of the cloud. It is clear that the star-forming clouds are rarely close to spherical. Only three objects in our sample, R5, R5wt and Z1, have a relatively round shape, with a tangential velocity that is only $\sim 30\%$ of that required for Keplerian motion. These clouds are similar in shape to the objects simulated by ABN02 and Yoshida et al. (2006). However, half of our objects, Z1, Z1wt, Z2 and Z2w, have a disk-like structure of varying size and thickness which is nearly rotational supported ($V_t/V_{Keplerian} > 0.6$), while one, Z2Wt, has a bar-like structure.

Density and temperature maps at the final time in the Z1 and the Z2wt objects are shown in Figures 8 and 9 respectively. The left and right panels give the density and temperature maps respectively. The top panels depict square regions of length $4 \times r_{200}$ and depth r_{200} in projection. In the lower panels, the scale has been adjusted to illustrate the disk in Z1 and the bar in Z2wt, with the projected velocity field superposed onto the density map. Both structures are shown face-on.

There are systematic differences between the internal structure of the main object and its surroundings in R5, Z1 and Z2wt. For the R5 object, the surrounding dark matter distribution is quite complex. There are 3 prominent objects connected to each other by filaments (see Fig 3) and the gas at the intersection of these filaments is shock-heated by infall. For the Z1 and Z2wt objects, the arrangement of the dark matter is simpler. These objects form at the intersection of only two filaments. For the gas distribution, the situation is the reverse: the gas around R5 is relatively featureless, but in Z1 and Z2wt, the inflowing gas has a complex structure. This is reflected also in the temperature maps of the Z1 and Z2wt objects which show a distinctly chaotic pattern.

The star-forming cloud in the R5 object is relatively spherical, as may be seen in Table 5, while the Z1 object has a disk-like structure extending out to a radius of $\sim 0.1\,$pc. The Z2wt object has a huge bar extending out to a radius of $\sim 1\,$pc. In both these objects the gas velocity fields are well organized, revealing a nearly circular pattern in Z1 and a vortical pattern around the bar in Z2wt. However, in the very inner regions of Z1, the gas has less rotational support (see Fig. 7) and is undergoing an inside-out collapse. It will be very interesting to study the fate of this gas in future work.

Disk-like structures have been seen in previous simulations of first stars by Bromm et al. (1999, 2002). These authors used constrained initial conditions and arbitrarily assigned a high value of the spin parameter to the simulated region. The disk in our simulation is substantially different from theirs. In Bromm et al. (1999, 2000), the disk-like structure formed shortly after virialization, then broke up rapidly into several disjointed gas clumps ranging in mass from 200 to $10^4\,M_\odot$. In our simulation which started from proper cosmological initial conditions, the gas acquires angular momentum self-consistently by tidal torques from surrounding structures, rather than being put in by hand as in Bromm et al. The disk forms at a later stage when the central gas density approaches $10^9 \mathrm{cm}^{-3}$, and there is no sign that the disk-like structure is unstable to fragmentation up to the time when we stop our simulation. This is because the disk is hot and thick, and so is pressure supported. We have checked that the Toomre Q parameter,

$$Q = \frac{\Omega c_s}{\pi G \Sigma}, \tag{4}$$

of the Z1 disk lies in the range $2 - 3$ which also suggests that it is stable against perturbations. Here, Ω is the local angular frequency, c_s is the sound speed, and Σ is the surface density.

The Z1wt and Z2w simulations also formed thick disks and careful inspection reveals the presence of spiral arms, as may be seen in Fig. 10. The associated asymmetric density fluctuations will produce gravitational torques that will help transport angular momentum outwards efficiently.

The processes that drive the different morphologies exhibited by the star-forming clouds in our simulations remain unclear. We have been unable to find any correlation between morphology and the various global properties that we have examined and we have found no clear relationship to the merging history of the host dark halo. We defer a more detailed study of the origin of the morphologies of star-forming clouds to a future study.

5.3 Accretion rate

The rate of mass accretion within the pre-stellar cloud is an important quantity which governs the evolution of the protostar. The growth of the protostar can be estimated by the mass accretion rate, $\dot{M}$, via

$$M_*(t) = M_{\rm proto} + \int_0^t \dot{M}(t)\,\mathrm{d}t, \tag{5}$$

where $M_{\rm proto}$ is an initial protostellar mass. In our simulations, we have neither enough resolution nor a sufficiently complete physical model to be able to resolve the initial protostar. One-dimensional hydrodynamic simulations including all the relevant physics suggest that the protostar mass is of order a few Jupiter masses (Omukai& Nishi 1998; Ripamonti et al. 2002).

Ideally, we need to follow the protostellar evolution along with the accretion in order to obtain a reliable final mass for the star. However, the coupled evolution of the

	R5	R5wt	Z1	Z1w	Z1wt	Z2	Z2w	Z2wt
$M_{\rm core}[{\rm M}_\odot]$	200	250	1000	1000	2000	3000	2000	4000
$R_{\rm core}$[pc]	0.03	0.05	0.28	0.48	0.99	1.78	0.88	1.1
$q = b/a$	0.83	0.83	0.87	0.96	0.83	0.87	0.97	0.40
$s = c/a$	0.50	0.53	0.28	0.70	0.32	0.30	0.33	0.11
V_t/V_K	0.3	0.3	0.7	0.3	0.6	0.6	0.7	-

Table 5. The principal axes ratios, $q = b/a$ and $s = c/a$, for our 8 simulations, where $a > b > c$. Here, the edge of the star-forming cloud is defined as the outer radius of the region in which the orientation of the specific angular momentum is roughly constant. This radius is denoted by $R_{\rm core}$; $M_{\rm core}$ is the enclosed gas mass within it.

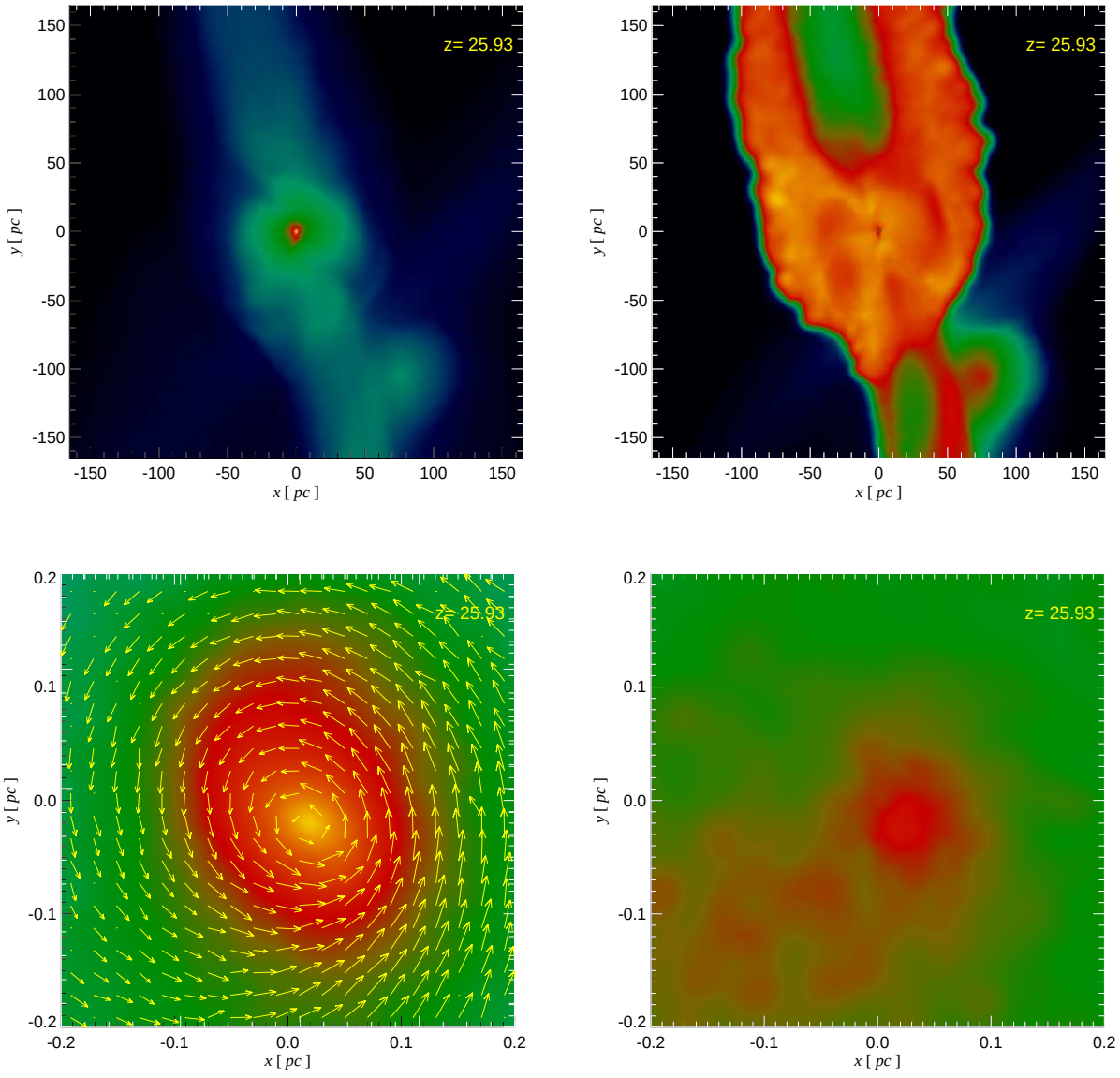

Figure 8. Density (left) and temperature (right) maps for the z1 simulation which has a disk-like structure at the final time. The upper panel shows a slice of side $4r_{vir}$ and depth r_{vir}. The bottom panel shows a cubic region of side 0.4 pc chosen to include the disk-like structure which is shown face-on. The projected velocity field is superposed onto the density map.

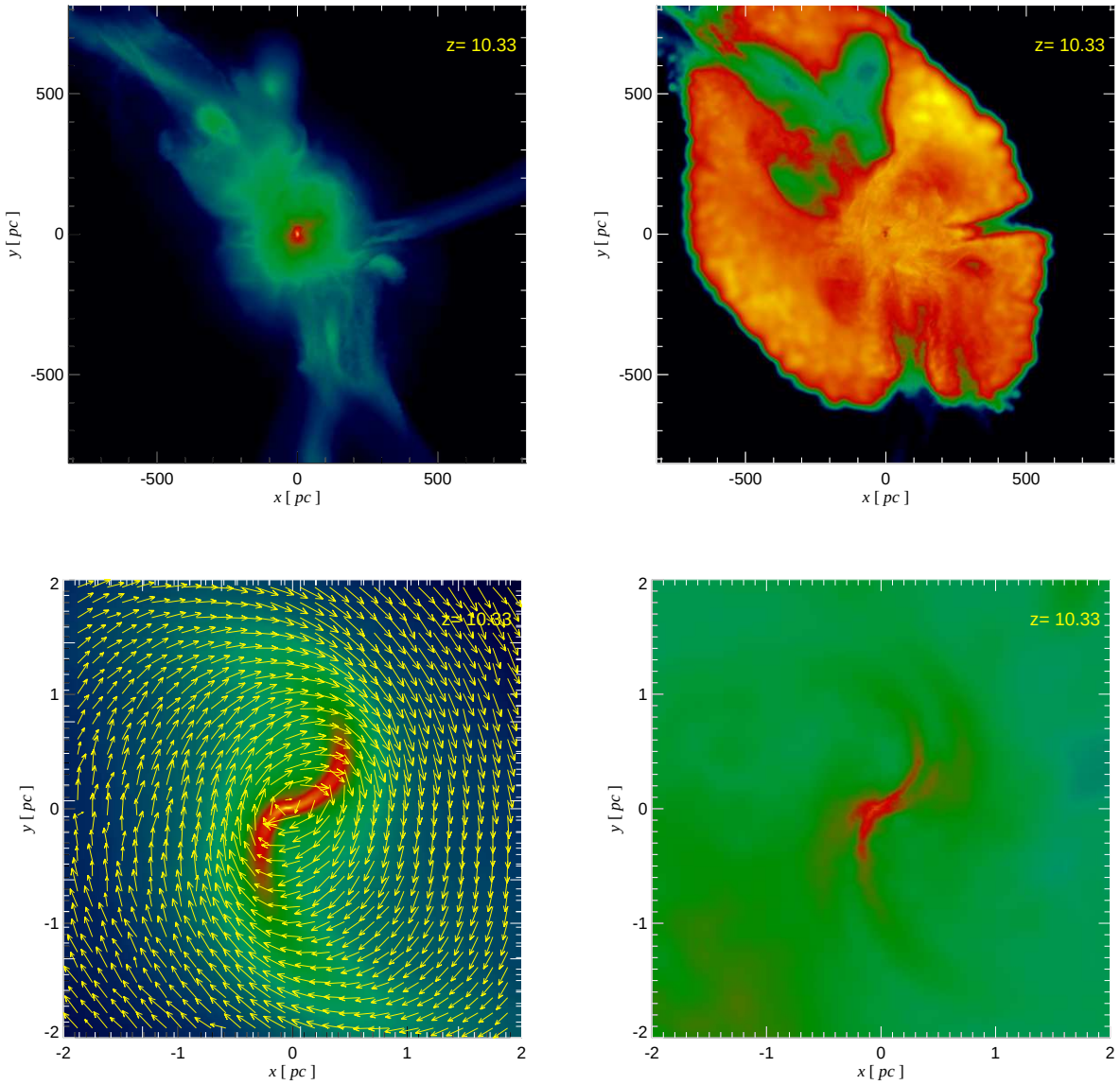

Figure 9. Density (left) and temperature (right) maps for the Z2wt simulation which has a bar-like structure at the final time. The upper panel shows a slice of side $4r_{vir}$ and depth r_{vir}. The bottom panel shows a cubic region chosen to include the bar-like structure which is shown face-on. The projected velocity field is superposed onto the density map.

protostar and the accreting envelope gas is a very complex physical problem which has not been solved so far, even in one-dimensional radiative hydro–dynamical simulations. At present, to estimate plausible stellar masses one needs to resort to either analytical collapse solutions (e.g. Larsen 1968; Penston 1967, Shu 1977), to detailed protostellar calculations with constant accretion rates (Omukai & Palla 2001;2003), or to estimates based on the instantaneous accretion rate from a particular numerical simulation (Tan & McKee 2003; Omukai & Palla 2003; Yoshida et al. 2006; but see Bromm & Loeb 2004 for a slightly different approach). Here we present the instantaneous accretion rates found in our own simulations.

In Figure 11, we show the instantaneous accretion rate, as a function of enclosed gas mass, for our 8 simulations. Here, the accretion rate is defined as $\dot{M}(r) = 4\pi r^2 \rho(r)|v_{\rm rad}|$ and is calculated at the time when the central gas density has reached a value of $n_{\rm H} \sim 10^{10}{\rm cm}^{-3}$. Since the accretion rate depends on the local gas density and on the gas infall velocity, we expect a considerable scatter from one object to another due to very different gas motions and variations in the local density.

The R5, R5wt, Z1w and Z2wt objects have the largest instantaneous accretion rates amongst all the simulations, and, at the same time, they also have the least rotational support. The Z1, Z1wt, Z2, and Z2W objects have the smallest accretion rates because their disk-like structures slow down the gas infall rate. Thus, the accretion time allows our simulated objects to be roughly divided into two populations, depending on the morphology of the star-forming

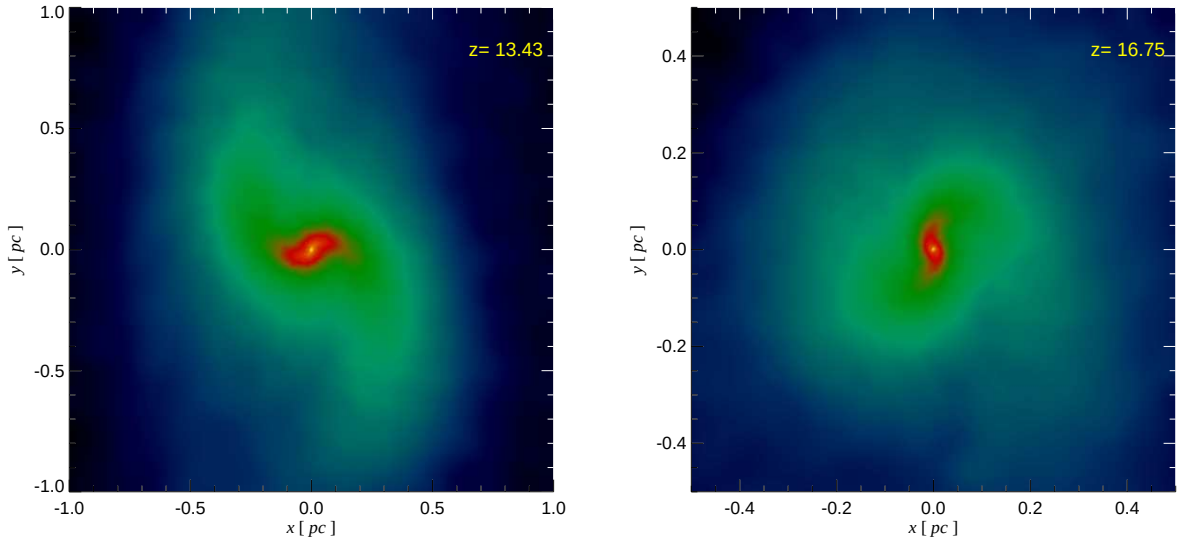

Figure 10. Density maps for the Z1wt and the Z2w simulations which have a disk-like structure at the final time. These images clearly reveal the presence of spiral arms contained in the disk-like structure. The projection is in an arbitrary direction.

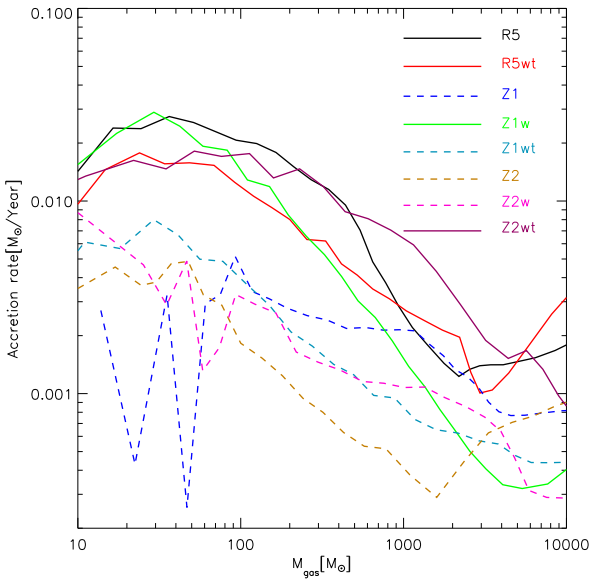

Figure 11. Accretion rate, $\dot{M(r)} = 4\pi r^2 \rho(r) v_{\rm infall}$, as a function of enclosed gas mass for our 8 simulations. Here, the accretion rate is computed at the time when the central gas density has reached a value of $n_{\rm H} \sim 10^{10}{\rm cm}^{-3}$. The accretion rates for objects with a central disk-like structure are ploted as dahsed lines, while objects with other morphologies are plotted as solid lines.

clouds. The accretion time for rotationally supported disks is much longer than for the other morphologies.

Omukai & Palla (2003) identified a critical accretion rate of $\sim 4 \times 10^{-3}\,{\rm M}_\odot{\rm yr}^{-1}$ (the thick solid line in Figure 11) for a star to form. This rate is physically motivated by the fact that the protostar luminosity cannot exceed the Eddington limit; otherwise a radiation-driven expansion of the protostar would halt or even reverse the accretion when the star reaches a mass of $\sim 100\,{\rm M}_\odot$. Note that with this high accretion rate, the star may in fact start burning hydrogen well before the accretion slows down, so that $M/\dot{M}$ becomes much longer than the lifetime of the star. Such an object would not be a zero-age main sequence mass. If the accretion rate is smaller than the critical rate, however, the star could continue to accrete gas after it settles onto the zero-age main sequence (ZAMS), allowing it to reach a larger final mass. In our simulations, objects without disks all have instantaneous accretion rates on scales corresponding to an enclosed mass of less than a few hundred solar masses that are a few times higher than the critical rate, while those with disk-like star-forming clouds have lower or comparable rates to the critical one.

Does this mean that our simulated objects with accretion rates larger than the critical value would be limited to a final mass of about $\sim 100\,{\rm M}_\odot$ by radiative feedback from their own protostars? To address this question, we carry out an experimental calculation to examine whether the instantaneous accretion rate is robust enough to serve as a reliable estimator of the theoretically expected final mass of the star. To this end, we examine whether the velocity structure of the gas in the protostellar environment changes rapidly, particularly whether the gas would spin up after further collapse which may slow down (or even halt) later accretion. For the R5 simulation, which has a star-forming cloud with little rotational support at our fiducial end state, we continued to integrate forward in time for another 1000 years (unlike ABN02 and Yoshida et al. (2006) who halted their simulation at this time). The ratio of the tangential velocity to the Keplerian rotational velocity at several times during this period is shown in Figure 12.

The red solid line with open diamonds refers to the final time when our physical model is still adequate. One can see that as the evolution is allowed to proceed, the gas cloud becomes increasingly rotationally supported and forms a ring-like structure at a length scale of ~ 0.02pc within one thou-

sand years, which is a short time in the lifetime of a protostar. While this evolution is not fully realistic because neither is the adopted inner boundary condition correct nor is the feedback generated by the protostar considered, it nevertheless highlights the fact that the velocity field in the protostellar environment can change rather rapidly. This suggests that it is hard to draw definitive conclusions regarding the likely mass of the star-forming cloud in the R5 halo based solely on the instantaneous accretion rate.

Continuing the integration of the other systems which have similar morphologies to R5 yields similar results: the accretion rate typically tends to become smaller as gas becomes more and more rotationally supported. By contrast, in the Z2wt object, whose star-forming cloud has a bar-like structure, the accretion rate rises at slightly later times when the asymmetrical mode of the bar transfers angular momentum outwards very rapidly and so boosts gas infall. As a result, gas accretion onto the protostar of the Z2w halo might be limited by the feedback effects discussed in Omukai & Palla (2003) and Tan & McKee (2003). Integrating the systems with a disk-like structure further in time, we find that the accretion rate falls even below that measured at the final reliable output time. We conclude that the instantaneous accretion is not a robust indicator of the mass of the final PoP-III star.

The instantaneous accretion rates within the radius containing 100 solar masses found in the simulations of ABN02 and Yoshida et al. (2006) are consistent with our estimates. Their rates lie within the scatter that we find in our set of eight simulations. Recently, O'Shea & Norman (2006b) carried out a set of simulations similar to ours using an AMR code. While they found, as we do, that there is considerable scatter in the instantaneous accretion rate from object to object, their scatter is an order of magnitude larger than ours. Another significant difference between their work and ours is that we find no correlation between the redshift of formation and the instantaneous accretion rate of our objects whereas they do. We do not know, at present, the reasons for these differences.

6 INFLUENCE OF THE BARYON FRACTION

It is interesting to examine how our choice of cosmological parameters affects the properties of primordial gas clouds. In particular, the baryonic matter density, or baryon fraction, may be one parameter which can signficantly affect the gas evolution. Naively, one would expect that the baryon fraction influences the gas collapse process, since both the production of molecular hydrogen and the cooling function at low densities depend strongly on density. Furthermore, initially the gas distribution in dark matter halos follows closely that of the dark matter component, with an enclosed baryonic fraction that should be close to the mean cosmic value (e.g. Lin et al. 2006). Thus, varying the baryon fraction may significantly change the density distribution of the gas within a halo.

Given the uncertainties that remain regarding the precise values of the basic cosmological parameters of our Universe (see the discussion in Spergel et al. 2006), in this section, we investigate the effects of varying the baryon fraction, $f_b = \Omega_b/\Omega_m$, on the formation of the first pro-stellar objects.

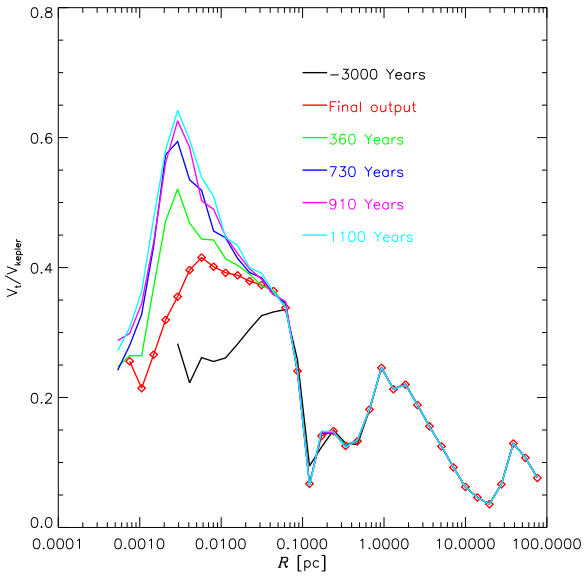

Figure 12. The ratio of the tangential velocity to the Keplerian circular velocity, as a function of radius, at several epochs for the R5 simulation. The red curve with open squares refers to our last trusted epoch when the optically thin assumption is still valid. The time intervals between the other outputs and this final time are indicated in the labels.

The precise values of the matter-density, Ω_m, of the dark energy component, Ω_Λ, and the shape and normalization of the initial power spectrum are all important for determining the abundance and the formation epoch of the first stars, but are less important than the baryon fraction in determining the properties of individual star forming clouds. We consider some of these other properties in the next section. A final reason for varying the baryon fraction is that it facilitates a direct comparison with the results of ABN02 who used a smaller value than we have assumed so far.

We have resimulated the Z1 object with three different choices for the baryon fraction. Our fiducial choice is $f_b = 2/15$, until recently, the value assumed in the standard (or "concordance") ΛCDM model. We compare this with the lower baryon fraction, $f_b = 0.06$, which was often used in the context of the now abandoned $\Omega_{\rm m} = 1$ standard CDM model assumed by ABN02. Finally, we also consider $f_b = 0.178$, as suggested by the latest WMAP and 2dFGRS results (Sanchez et al. 2005, Spergel et al. 2006). We refer to the simulations with lower and higher baryon fractions as as Z1lb and Z1hv respectively.

In Figure 13, we compare the radial profiles of the gas density, enclosed gas mass, temperature and radial velocity in the three simulations. The magenta dashed lines show the results of ABN02. The radially averaged physical properties of the Z1hb and Z1 simulations are generally very similar, although some small differences are apparent. For example, the density profile of Z1hb is $\sim 20\%$ higher than that of Z1 over much of the range shown. The differences are much larger for the lower baryon fraction simulation. On scales $0.1 - 1\,$pc, the gas density in Z1lb is roughly a factor of 2 lower than in the other simulations. The radial gas velocity of Z1lb is also very different from that of Z1 and

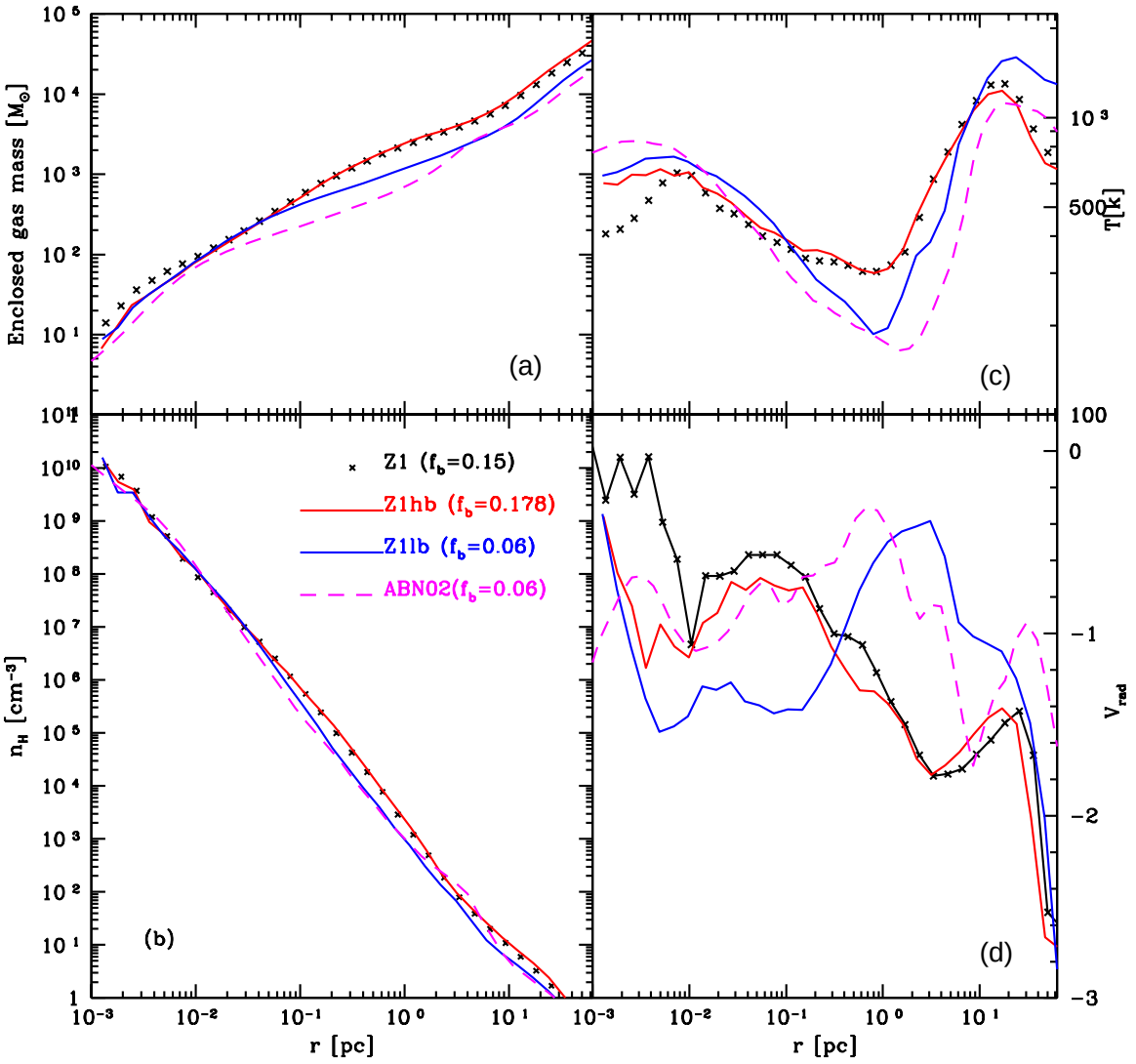

Figure 13. Comparison of various spherically averaged profiles in the Z1 simulation for different assumed baryon fractions. Panel (a): enclosed gas mass; panel (b): number density of hydrogen nuclei; panel (c): temperature; panel (d): radial velocity. The lines refer to different simulations as indicated by the label. The redshifts are $z = 25.93$ for the Z1 run, $z = 26.26$ for the Z1hb simulation, and $z = 24.26$ for the Z1lb run. Relative to the fiducial, $f_b = 2/15$, case, star formation in the higher baryon fraction simulation occurs ~ 2 million years earlier, while in the lower baryon fraction simulation, it is delayed by ~ 12 million years.

Z1lb. In fact, surprisingly, the disk-like structure has disappeared in the Z1lb simulation, although it is still present in the higher baryon fraction simulation, Z1hb. Finally, we note that matching the lower baryon fraction assumed by ABN02, as in Z1lb, produces much better agreement between our results and theirs.

We find that the baryon fraction influences the collapse time of the star-forming cloud quite significantly. Relative to Z1, the collapse proceeds slightly faster in Z1hb and much more slowly in Z1lb. In Z1hb, star formation occurs as early as $z = 26.26$ (that is 2 million years earlier than in Z1), while in Z1lb, it is delayed by 12 million years, to a redshift of $z = 24.26$. We conclude that a slight change in the baryon fraction does not affect the properties of star-forming clouds much, but changes by a factor $\simeq 2$ have a significant effect.

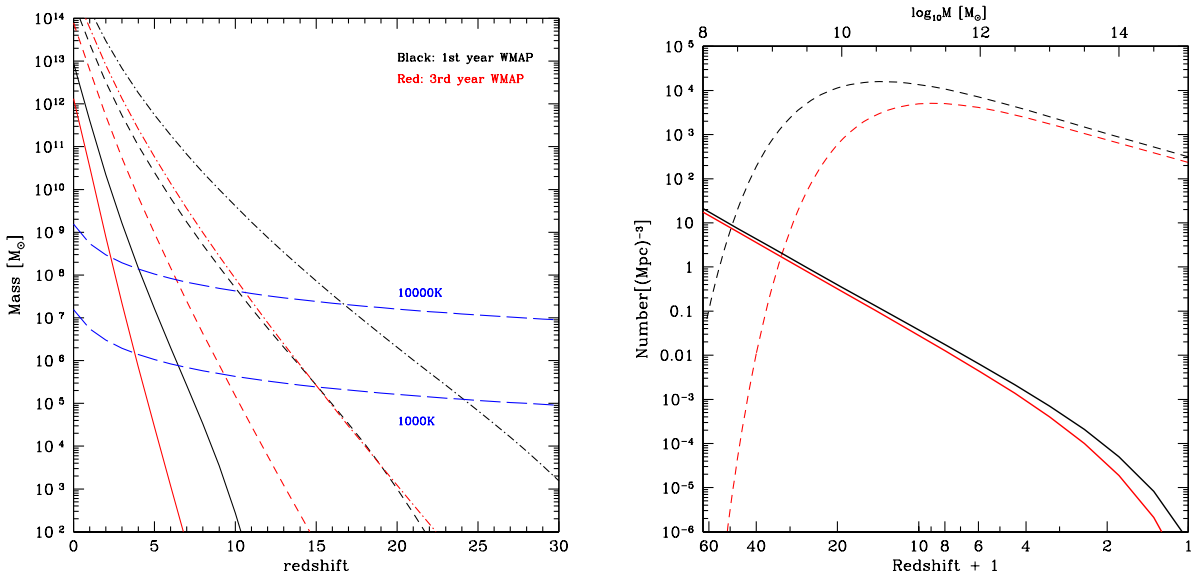

Figure 14. Left-hand panel: halo mass as a function of redshift. The solid lines corresond to the mass M_*, defined through $\nu = \sigma(M)/\delta_c = 1$; the dashed lines correspond to the mass of 2σ halos ($\nu = 2$); the dot-dashed lines correspond to the mass of 3σ ($\nu = 3$) halos. The black curves show results for cosmological parameters derived from the 2dFGRS and the first year WMAP data and the red curves for parameters derived from the 2dFGRS and three-year WMAP data (Sanchez et al. 2005, Spergel et al 2006). The two long-dashed blue lines show the halo mass which, at each redshift, has a virial temperature of more than 1000 K and 10000 K, respectively, as indicated by the labels. Right-hand panel: the predicted halo abundance in the two cosmologies. The solid lines show cumulative comoving number densities of halos more massive than a given mass as a function of redshift (upper axis). The dashed lines show the predicted comoving number density of halos that have a virial temperature exceeding 1000 K as a function of redshift (lower axis). This is roughly the critical temperature at which gas can start efficient cooling by molecular hydrogen.

7 ABUNDANCE OF STAR-FORMING HALOS

So far, we have concentrated on the physical processes that lead to the formation of the first protostars in a ΛCDM universe. We now turn to a discussion of the abundance of early star-forming halos and its dependance on cosmological parameters in a ΛCDM universe. As we have shown in Section 3, the basic principles that determine the formation paths of the first protostars are simple: once gas is heated up to a temperature of around 1000 K, the production of molecular hydrogen is boosted sufficiently for the gas cloud to cool very rapidly. The ensuing collapse proceeds faster if it takes place in a halo at higher redshift because in that case the gas starts off with a higher density and temperature and a shorter dynamical time.

As shown in Figures 1 and 5, the virial temperature provides a reasonable estimate of the initial temperature of the star-forming material at the time when it begins to settle into the halo. In Figure 14, we show the abundance of objects with virial temperature above 1000 K. Note that the gas in a halo with this temperature is predicted to *start* collapsing at this time, but the collapse process itself, eventually yielding a protostellar object, takes a further $\sim 10^6 - 10^8$ years. This corresponds to is significant interval in redshift, $\Delta z \sim$ of a few, depending on the exact redshift.

The first stars in the standard ΛCDM cosmology are often assumed to form typically at redshifts between $z = 20$ and $z = 30$ because 3σ halos with a virial temperature of $\simeq$ 1000 K collapse in this redshift range. In the left-hand panel of Figure 14, we plot the abundance of 1σ, 2σ and 3σ halos as a function of redshift. A similar figure has been shown in a number of previous studies (e.g. Barkana & Loeb 2001) but here we compare results obtained for two choices of cosmological parameters, those inferred by combining the galaxy power spectrum of the 2dFGRS with the first-year and three-year WMAP data respectively. In the figure, 1σ halos are shown with solid lines, 2σ halos with short-dashed lines and 3σ with dot-dash lines. The two long-dashed blue lines show the halo mass which, at each redshift, has a virial temperature of more than 1000 K and 10000 K, respectively.

As a consequence of the significant suppression of power on small scales in the 2dFGRS+three-year WMAP cosmology (due to a lower value of σ_8 and a red tilt in the primordial power spectrum index), the curve for the 3σ halos in this cosmology is shifted so much that it nearly coincides with that for the 2σ halos in the older cosmology. The curve for halos which have a virial temperature exceeding 1000 K crosses the curve for 3σ halos in the 2dFGRS+three-year WMAP cosmology at $z \sim 15$ instead of at $z \sim 25$ as in the older cosmology.

The dramatic changes in the number of halos that can host the first stars arising from the relatively small change in the values of the cosmological parameters in the 2 models we considering are illustrated in the right-hand panel of Figure 14. Here, the comoving abundance of potential first-star-bearing halos, i.e. those with a virial temperature exceeding 1000 K is plotted as a function of redshift (labelled along

the lower axis) for the two sets of cosmological parameters (distinguished by the two colours as in the left panel). For reference, we also plot the comoving abundance of all halos at the present day, as a function of halo mass (labelled along the upper axis), based on the fitting formula of Sheth, Mo & Tormen (2000), which works reasonably well for large masses (Jenkins et al. 2001; Springel et al. 2005; Reed et al. 2006).

The abundance of potentially star-forming halos differs dramatically in the two cosmologies at redshifts greater than $z = 10$. At redshift $z = 50$, the predicted abundance of halos capable of molecular cooling is ~ 7 orders of magnitudes lower in the 2dFGRS+three-year WMAP cosmology than in the older 2dFGRS+first-year WMAP cosmology. As cosmic time increases, the predicted abundance of star-forming halos increases very rapidly, as noted by G05. By redshift $z \sim 35$, the abundance of halos with $T_{\rm vir} > 1000$K has increased by 6 orders of magnitude, making it comparable in the cosmology that uses the 3-year *WMAP* data to that of dwarf galaxies at the present day. By redshift $z \sim 15$, the abundance of such objects is 1000 times higher than that of $10^8\,{\rm M}_\odot$ halos today. It is clear that the current uncertainty in the values of the cosmological parameters, particularly σ_8, is a major source of uncertainty for the predicted abundance and evolution of Pop-III stars.

8 SUMMARY AND DISCUSSION

In this paper, we have presented a large set of cosmological SPH simulations of the formation of the first stars. Our simulations reach sub-solar mass resolution and include an accurate and detailed chemistry network to treat radiative cooling by molecular hydrogen. Our large suite of simulations allows us to investigate the scatter in the properties of star-forming clouds and the redshift dependence of their formation process. Our simulations stop when the central gas density has reached $n_{\rm H} \sim 10^{10}{\rm cm}^{-3}$, the point at which our assumption that the gas is optically thin begins to break down.

Despite the complexities in detailed formation paths, our simulations suggest a relatively simple picture leading up to the development of the first star-forming clouds. Once primordial gas is heated to $\sim 1000\,{\rm K}$, either by shocks or by adiabatic compression, the production of molecular hydrogen is boosted. When the molecular fraction reaches a few times 10^{-4}, the gas cools rapidly and settles to the centre of the gravitational potential well of the halo. Our simulations bear out the same sequence of events sketched in earlier semi-analytical work by Tegmark et al. (1997) and seen in the detailed simulations of Fuller & Couchman (2000), Machacek et al. (2001) and Yoshida et al. (2003). Our main results may be summarized as follows:

(1) The formation path of Pop-III stars is broadly similar in all halos, independently of collapse redshift and environment. However, the timescale for the collapse differs systematically depending on the redshift at which the collapse takes place. The gas condenses more rapidly into stars at high redshift and so the formation timescale can differ by factors as large as 20 for halos that collapse between redshifts $z \sim 50$ and $z \sim 15$. For example, for the R5 object which starts to form at $z \sim 50$, the collpase takes as little as a few million years whereas for the Z2wt halo, which began to form at $z \sim 15$, the collapse took 100 million years.

(2) The spherically averaged radial gas density profiles of the star-forming clouds agree well with each other up to a radius of $\sim 10\,{\rm pc}$. The profiles exhibit a power-law distribution $\rho \propto r^{-2.2-2.3}$ which extends over 10 orders of magnitude in density and is independent of formation redshift and environment. The molecular hydrogen fractions and temperature structures are also very similar. The main reason why these similarities are present is that once the gas has started to collapse, it largely isolates itself from the rest of the evolving halo and so the final state of the star-forming cloud becomes largely insensitive to the global properties of the host halo such as its virial mass, temperature or spin.

(3) Despite the similarity in the radial profiles of gas density, temperature, and molecular hydrogen fraction, the velocity field of the gas can differ significantly from object to object.

(5) At the moment when our simulations stop, the star-forming clouds exhibit a variety of morphologies. Some of them are nearly rotationally supported disks, others resemble flattened spheroids, while others possess self-gravitating bars. The instantaneous accretion rate onto the central region distinguishes between two kinds of star-forming clouds. Those with a disk-like structure have the smaller accretion rates, while those that resemble flattened spheroids or possess bars have the larger accretion rates. The scatter in accretion rate can be more than a factor of 10 and is related to the morphology of the cloud.

(6) A higher baryon fraction increases the gas density everywhere within a halo and speeds up the formation of the first stars.

(7) The predicted abundance of Pop-III halos in the ΛCDM model varies dramatically depending on whether one assumes the cosmological parameters derived using either the first year or the three-year WMAP data. For example, the abundance of objects similar to our R5 halo differs by 7 orders of magnitudes at redshift 50 in the two cosmologies.

At the moment when our simulations stop, i.e. when $n_{\rm H}$ reaches a value $\sim 10^{10}{\rm cm}^{-3}$, none of the central star-forming clouds have fragmented. This is in agreement with earlier simulations (ABN02; Bromm et al. 2002; O'Shea & Norman 2006a,b; Yoshida et al. 2006). At this time, all our simulated objects experience a much higher instantaneous accretion rate onto their central region than is common in protostars today. If fragmentation does not occur and the accretion does not slow down significantly, these objects are likely to bear a star of more than a few tens of solar masses which would have accumulated on a timescale of $\sim 10^5$ years. However, the velocity structure around the protostars, and thus the instantaneous accretion rate, varies greatly from object to object, and this suggests that the final masses of the first stars may not lie in a narrow range. However, it is unclear whether the differences in the instantaneous accretion rates will be directly proportional to the final mass of the stars because the velocity structure of the gas in the protostellar environment changes very rapidly with time.

The fate of the star-forming clouds resolved in our simulations is unclear. In order to reach stellar densities, the gas clouds must still collapse by more than four orders of magnitude in radius and this requires efficient transport of

angular momentum. This is a complicated problem and the various morphologies of the star-forming clouds we find suggest that its solution may involve more than a single physical process. One way to transport angular momentum outwards and facilitate further efficient accretion is through gravitational torques generated by spiral density fluctuations. Only 3 of our 8 objects exhibit spiral structure in the central regions at the time when we halt our simulations and it is unclear if the other objects will also develop spiral structure later on. A further and critical complicating factor is the uncertain effect of feedback generated by the protostar on the dynamics of the accreting gas.

Because of all of the complications just discussed, the masses of the first stars remain uncertain. A greater level of complexity than is possible with the current generation of simulations will be required to answer this fundamental question. These simulations will need to be able to model, in a self-consistent way, the dynamics of the accreting gas, the evolution of the protostar and the various radiative, chemical and mechanical feedback effects that are likely to be at play in the formation of the first generation of stars.

ACKNOWLEDGEMENTS

The simulations described in this paper were carried out on the Blade Center cluster of the Computing Center of the Max-Planck-Society in Garching and on the Cosmology Machine of the Institute for Computational Cosmology in Durham. We thank Shude Mao, Darren Reed and Yuexing Li for a careful reading of an earlier version of the draft. LG is particularly grateful to Simon White for extensive discussions and many constructive suggestions. CSF ackowledges a Royal Society Wolfson Research Merit Award. The work is supported in part by the Grants-in-Aid for Young Scientists (A) 17684008 (NY) by the Ministry of Education, Culture, Science and Technology in Japan.

REFERENCES

Abel T., Anninous P., Norman M. L., Zhang Y., 1997, New Astronomy, 2, 181
Abel T., Bryan G. L., Norman M. L., 2000, ApJ, 540, 39
Abel T., Bryan G. L., Norman M. L., 2002, science, 2002, 295, 93
Barkana R., Loeb A., 2001, Phys Rep., 349, 125
Bate M. W., Burkert A., 1997, MNRAS, 288, 1060
Bromm V., Coppi P. S. & Larsen R. B., 1999, ApJ, 527, L25
Bromm V., Coppi P. S. & Larsen R. B., 2002, ApJ, 575, 111
Bonnor W. B., 1956, MNRAS, 116, 351
Ciardi B., Ferrara A., 2005, Space Sci. Rev., 116, 625
Cole, S., Percival, W. J., Peacock, J. A., Norberg, P., Baugh, C. M., Frenk, C. S., Baldry, I., and 24 others, 2005, MNRAS, 362, 505
Couchman H .M. P., Rees M. J., 1988, MNRAS, 221, 53
Doroshkevich A. G., Zel'Dovich Y. B., Novikov I. D., 1967, Astronomicheskii Zhurnal, 44, 295
Ebert R., 1955, Z. Astrophys., 37, 217
Fan X. et al. 2001, AJ, 122, 2833
Fuller T. M., Couchman H. M. P., 2000, ApJ, 544, 6
Galli D., Palla F., 1998, A&A, 335, 403
Gao L., White S. D. M., Jenkins A., Frenk C. S., Springel V., 2005, MNRAS, 363, 379
Glover S., 2005, Space Sci. Rev., 117, 445
Haiman Z., Thoul A. A., Loeb A., 1996, ApJ, 464, 523
Hirata C. M., Padmanabhan N., 2006, MNRS submitted, 2006, astro-ph/0606437
Hollenbach D., McKee C. F., 1979, ApJ, ApJS, 41, 555
Jenkins A., Frenk C. S., White S. D. M., Colberg J. M., Cole S., Evrard A. E., Couchman H. M. P. Yoshida N., 2001, MNRAS, 321, 372
Larson R. B., 1969, MNRAS, 145, 271
Lin W. P., Jing Y. P., Mao S., Gao L., McCarthy I, 2006, ApJ in press, astro-ph/0607555
Matsuda T., Sato H., Takeda H., 1969, Prog. Theor. Phys., 42, 219
Machacek M. E., Bryan G. L., Tom A., 2001, ApJ, 548, 509
Nakamura F., Umemura M., 2002, ApJ, 569, 549
Omukai K., Nishi R., 1998, ApJ, 508, 141
Omukai K., Palla F., 2001, ApJ, 561, L55
Omukai K., Palla F., 2003, ApJ, 589, 677
O'Shea B. W., Abel T., Whalen D., Norman M. L., 2005, ApJ, 628, L5
O'Shea B. W., Norman M. L. 2006a, ApJ submitted, astro-ph/0602319
O'Shea B. W., Norman M. L., 2006b, ApJ submitted, astro-ph/0607013
Peebles P. J. E., Dicke R. H., 1968, ApJ, 154, 891
Peebles P. J. E., 1993, *Principles of Physical Cosmology*, Princeton University Press
Penston M. V., 1969, MNRAS, 144, 425
Reed D. S., Bower R., Frenk C. S., Gao L., Jenkins A., Theuns T., White S. D. M, 2005, MNRAS, 363, 379
Reed D. S., Bower R., Frenk C. S., Jenkins A., Theuns T., 2006, MNRAS submitted, astro-ph/0607150
Ripamonti E., Haardt F., Ferrara A., Colpi M., 2002, MNRAS, 334, 401
Ripamonti E., Abel T., 2004, MNRAS, 348, 1019
Ripamonti E., Abel T., 2005, preprint, astro-phy/0507130
Sanchez A. G., Baugh C. M., Percival W. J., Peacock J. A., Padilla N. D., Cole S., Frenk C. S., Norberg P., 2006, MNRAS, 366, 189
Spergel et al., 2006, ApJ submitted, ArXiv:astro-ph/0603449
Springel V., 2005, MNRAS, 364, 1105
Springel V. et al., 2005, Nat, 435, 639s
Sheth R. K., Mo H. J., Tormen G., 2004, MNRAS, 323, 1
Shu F. H., 1977, ApJ, 214, 488
Silk J., 1983, MNRAS, 205, 705
Silk J., Langer M., 2006, MNRAS submitted, astro-ph/0606276
Tan J. C., McKee C. F., 2004, ApJ, 603, 383
Tegmark M., Silk J., Rees M. J., Blanchard A., Abel T., Palla F., 1997, ApJ, 474, 1
White S. D.M., Springel V., 2000, The First Stars. Springer-Verlag, Berlin P. 237
Yoshida N., Abel T., Hernquist L., Sugiyama N., 2003a, ApJ, 592, 645
Yoshida N., Sugiyama N., Hernquist L., 2003, MNRAS, 344, 481
Yoshida N., Omukai K., Herquist L., Abel T., 2006, ApJ in press, astro-ph/0606106

APPENDIX A: EVOLUTION OF VELOCITY PROFILES OF THE R5 OBJECT

Figure A1 is the evolution of velocity profiles of the R5 object.

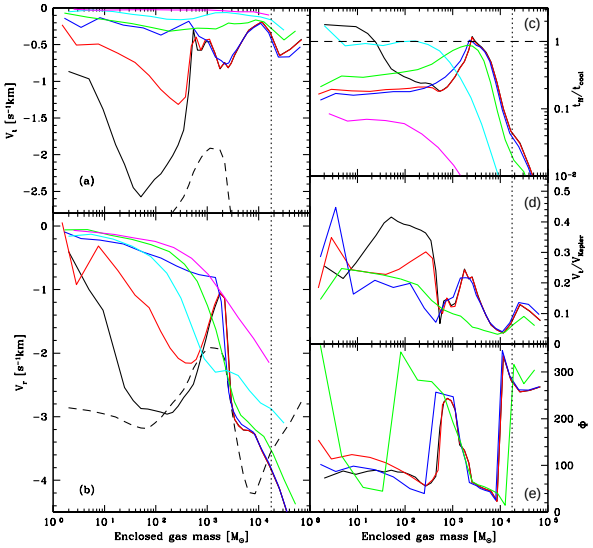

Figure A1. Radially averaged profiles of velocity and angular momentum related physical quantities as a function of enclosed gas mass for 5 output times of the R5 object. The lines correspond to the same times as in Figure 3. Panel (a): Negative tangential velocity profiles. The dashed lines in this panel and panel (b) refer to negative sound speed. Panel (b): Radial velocity profiles. Panel (c): The ratio of free-fall time to cooling time. Panel (d): The ratio of tangential velocity to the required Keplerian velocity $v_{Kepler} = (GM/r)^{1/2}$. Panel (e): The orientation of angular momentum. Note that only the angle ϕ is shown. The vertical doted lines in all panels indicate the enclosed gas mass within the virial radius. Note that only the last four outputs in panel (d) and (e) are shown, for clarity.

APPENDIX B: VELOCITY PROFILES OF 5 OBJECTS

Figure B1 is the same plot as Figure 7 but are for other 5 simulations.

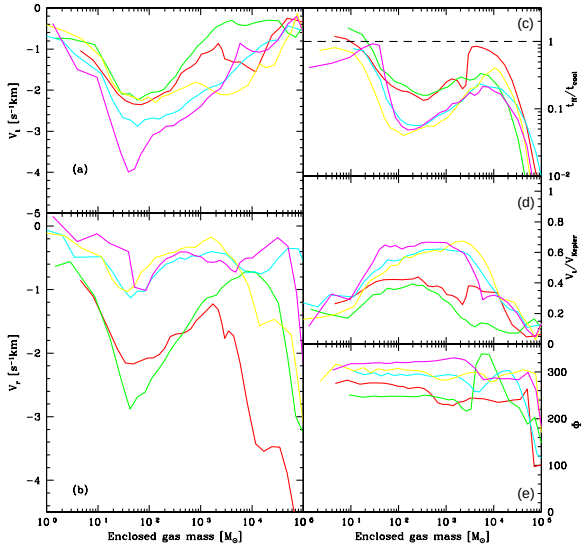

Figure B1. The same plots as in Figure 7 but for a different set of 5 simulations taken from our suite of runs: R5wt, Z1w, Z1wt, Z2 and Z2w. Panel (a): Negative tangential velocity profiles. Panel (b): Radial velocity profiles. Panel (c): The ratio of the free-fall time to the cooling time. Panel (d): The ratio of the tangential velocity to the Keplerian velocity $v_{Kepler} = (GM/r)^{1/2}$. Panel (e): The orientation of the angular momentum profiles. Note that only the angle ϕ is shown. The lines are the same as in Figure 6.